

Fast Proximal Gradient Methods for Nonsmooth Convex Optimization for Tomographic Image Reconstruction

Elias S. Helou, Marcelo V. W. Zibetti, and
Gabor T. Herman

the date of receipt and acceptance should be inserted later

Abstract The Fast Proximal Gradient Method (FPGM) and the Monotone FPGM (MFPGM) for minimization of nonsmooth convex functions are introduced and applied to tomographic image reconstruction. Convergence properties of the sequence of objective function values are derived, including a $O(1/k^2)$ non-asymptotic bound. The presented theory broadens current knowledge and explains the convergence behavior of certain methods that are known to present good practical performance. Numerical experimentation involving computerized tomography image reconstruction shows the methods to be competitive in practical scenarios. Experimental comparison with Algebraic Reconstruction Techniques are performed uncovering certain behaviors of accelerated Proximal Gradient algorithms that apparently have not yet been noticed when these are applied to tomographic image reconstruction.

Keywords Computerized tomography imaging, Convex optimization, Proximal gradient methods, Iterative algorithms.

Mathematics Subject Classification 65K05, 68U10, 90C25, 90C06, 92C55, 94A08

1 Introduction

In this paper we introduce the Fast Proximal Gradient Methods (FPGM) for the solution of convex minimization problems of the form

$$\min \quad \Psi(\mathbf{x}) := f(\mathbf{x}) + \phi(\mathbf{x}), \quad (1)$$

where $f: \mathbb{R}^n \rightarrow \mathbb{R}$ is a smooth convex function with Lipschitz continuous gradient and $\phi: \mathbb{R}^n \rightarrow \mathbb{R}$ is a proper convex function. It is not assumed that ϕ is smooth. From now on, the symbols f and ϕ will always represent functions satisfying these assumptions.

Many practical problems fit this general model. In particular, for image reconstruction from tomographic data, $f(\mathbf{x})$ is usually going to be a measure of consistency,

Elias S. Helou, Instituto de Ciências Matemáticas e de Computação, elias@icmc.usp.br
Marcelo V. W. Zibetti, Center for Advanced Imaging Innovation and Research (CAI²R), New York University School of Medicine, Marcelo.WustZibetti@nyumc.org
Gabor T. Herman, PhD Program in Computer Science, City University of New York, gabortherman@yahoo.com

according to the data acquisition model, of image \mathbf{x} with the data coming from the scanner whereas $\phi(\mathbf{x})$ is a measure of structure. For example, ϕ could enforce sparsity, smoothness, or some other desirable *a priori* information known about the image being reconstructed.

The algorithms we propose here lie between the Optimized Iterative Shrinkage-Thresholding Algorithm (OISTA) presented and experimented with in [18], but for which no convergence proof exists, and the Overrelaxed Monotone Fast Iterative Shrinkage-Thresholding Algorithm (OMFISTA) [25], for which convergence proofs do exist. One contribution of the present paper is a better understanding of the convergence properties of these algorithms. We get there by increasing the range of allowed parameters values for OMFISTA, consequently providing a way of justifying convergence of OISTA. We exhibit numerical experimentation using FPGM for computerized tomography image reconstruction [13] with both real and synthetic data and compare it with other methods from the viewpoint of convergence speed and image quality.

The paper is organized as follows. The remaining of the present section is dedicated to introduce the mathematical elements that will be used in the construction of the algorithm. Section 2 contains a non-extensive literature review about the subject of fast proximal gradient methods and fast first-order methods. The new algorithm is introduced in Section 3 and its convergence is analyzed in Section 4. Numerical experiments are presented in Section 5. Finally, Section 6 brings our conclusions and delineates plans for future work.

1.1 Proximal Operators

Proximal operators are useful tools for convex optimization, presenting an interesting balance between abstract power and practical applicability. Given a proper convex function $\phi : \mathbb{R}^n \rightarrow \mathbb{R}$ and a positive real number L , the L -proximal point of ϕ from a point $\mathbf{x} \in \mathbb{R}^n$ is defined as:

$$\text{prox}_{\phi,L}(\mathbf{x}) := \arg \min_{\mathbf{y} \in \mathbb{R}^n} \left\{ \phi(\mathbf{y}) + \frac{L}{2} \|\mathbf{y} - \mathbf{x}\|^2 \right\}. \quad (2)$$

We will, when there is no risk of confusion, refer to the L -proximal point of ϕ from $\mathbf{x} \in \mathbb{R}^n$ simply as the proximal point.

Although the computation of the proximal point involves a minimization, in many cases of interest this computation can be performed in a finite number of simple steps. Examples of functions ϕ that allow efficient closed-form representations of $\text{prox}_{\phi,L}$ include the ℓ_1 norm of an orthonormal transformation of a vector, that is, $\phi(\mathbf{x}) = \|Q\mathbf{x}\|_1$ where $Q \in \mathbb{C}^{n \times n}$ with $Q^*Q = I$, and the nuclear norm of a matrix $M \in \mathbb{C}^{m \times n}$, i.e., $\phi(M) = \|M\|_* = \sum_{i=1}^{\min\{m,n\}} |\sigma_i|$, where the σ_i are the singular values of M . For some other important functions, such as the Total Variation (*TV*), there are effective iterative procedures than can quickly approximate $\text{prox}_{\phi,L}(\mathbf{x})$ [3].

1.2 Proximal Gradient Methods

Let us define the proximal gradient operator as:

$$P_{L,f,\phi}(\mathbf{x}) := \text{prox}_{\phi,L} \left(\mathbf{x} - \frac{1}{L} \nabla f(\mathbf{x}) \right). \quad (3)$$

For simplicity, we will omit f and ϕ from the notation unless the omission causes ambiguity. A Proximal Gradient Method (PGM) for the minimization of (1) is then given by an iterative process in which

$$\mathbf{x}_{k+1} = P_L(\mathbf{x}_k), \quad (4)$$

see [22]. For large enough L , these iterations converge, but they do so slowly, and rates of the kind $\Psi(\mathbf{x}_k) - \Psi(\mathbf{x}^*) = O(1/k)$, where $\mathbf{x}^* \in \mathbb{R}^n$ is a minimizer of Ψ , are often predicted theoretically and observed in practice.

For smooth problems of the form

$$\min f(\mathbf{x}), \quad (5)$$

Nesterov [20] introduced the Fast Gradient Method (FGM)

$$\mathbf{x}_k = \mathbf{y}_k - \frac{1}{L} \nabla f(\mathbf{y}_k), \quad (6)$$

where $\mathbf{y}_1 = \mathbf{x}_0$ and

$$\mathbf{y}_{k+1} = \mathbf{x}_k + \frac{t_k - 1}{t_{k+1}} (\mathbf{x}_k - \mathbf{x}_{k-1}), \quad (7)$$

with $t_1 = 1$ and $t_k = \left(1 + \sqrt{1 + 4t_{k-1}^2}\right)/2$. Later, Beck and Teboulle proved that the same algorithmic form leads to a fast proximal gradient algorithm, called Fast Iterative Shrinkage-Thresholding Algorithm (FISTA) [2, 3], when (6) is replaced by

$$\mathbf{x}_k = P_L(\mathbf{y}_k). \quad (8)$$

These fast algorithms have much better theoretical and practical convergence properties than a PGM, at only a small extra computational cost, specially in high-dimensional problems such as occur in computerized tomography image reconstruction [13].

2 Literature Review

The introduction of FISTA renewed interest in Nesterov's ideas because the separable smooth plus nonsmooth model has a wider application range than smooth minimization, including many image processing and reconstruction problems within the Compressive Sensing (CS) framework [5]. Nesterov introduced his seminal ideas by considering First-Order Methods (FOMs) for the solution of (5). A FOM is a method with an iterative step of the form:

$$\mathbf{x}_{k+1} = \mathbf{x}_k - \frac{1}{L} \sum_{i=0}^k h_{k+1,i} \nabla f(\mathbf{x}_i), \quad (9)$$

where $h_{k+1,i} \in \mathbb{R}$ for $k \in \mathbb{N}$ and $i \in \{0, 1, \dots, k\}$. For this class of methods, there is a smooth convex function f with Lipschitz continuous gradient such that the sequence of iterates of every FOM would satisfy [21]

$$f(\mathbf{x}_k) - f(\mathbf{x}^*) \geq \frac{3L \|\mathbf{x}_0 - \mathbf{x}^*\|^2}{32(k+1)^2}, \quad (10)$$

thereby establishing a lower bound for the worst case scenario. On the other hand, the optimality gap, that is, the difference between the objective function value at the current iteration and the optimal objective function value, of the FGM was shown to be bounded by

$$f(\mathbf{x}_k) - f(\mathbf{x}^*) \leq \frac{2L \|\mathbf{x}_0 - \mathbf{x}^*\|^2}{(k+1)^2}. \quad (11)$$

Since FGM is a FOM, this algorithm has a convergence rate in terms of reduction of the objective function value with optimal leading exponent. However, the difference between the coefficients in the bounds (10) and (11) left hope for improvement of the convergence rate of FOMs.

More recently, Kim and Fessler [18] refined an approach by Drori and Teboulle [6] and obtained a method called Optimized Gradient Method (OGM) with the proven property that

$$f(\mathbf{x}_k) - f(\mathbf{x}^*) \leq \frac{L \|\mathbf{x}_0 - \mathbf{x}^*\|^2}{(k+1)^2}, \quad (12)$$

with iterations given by

$$\mathbf{x}_k = \mathbf{y}_k - \frac{1}{L} \nabla f(\mathbf{y}_k), \quad (13)$$

$$\mathbf{y}_{k+1} = \mathbf{x}_k + \frac{t_k - 1}{t_{k+1}} (\mathbf{x}_k - \mathbf{x}_{k-1}) + \frac{t_k}{t_{k+1}} (\mathbf{x}_k - \mathbf{y}_k). \quad (14)$$

The generalization of FGM to the nonsmooth case came when Beck and Teboulle [2] showed that the gradient step can be replaced by a proximal gradient step leading to the FISTA

$$\mathbf{x}_k = P_L(\mathbf{y}_k), \quad (15)$$

$$\mathbf{y}_{k+1} = \mathbf{x}_k + \frac{t_k - 1}{t_{k+1}} (\mathbf{x}_k - \mathbf{x}_{k-1}). \quad (16)$$

FISTA, similarly to FGM, satisfies

$$\Psi(\mathbf{x}_k) - \Psi(\mathbf{x}^*) \leq \frac{2L \|\mathbf{x}_0 - \mathbf{x}^*\|^2}{(k+1)^2}. \quad (17)$$

A monotone version of FISTA, called MFISTA was also developed [3], which shares with FISTA the same bound on the optimality gap. Kim and Fessler successfully experimented with a version of the OGM where the gradient step is replaced by the proximal gradient step [17]. Although numerically the algorithm so obtained behaved well, no theoretical convergence proof was provided.

In the present paper we prove convergence of algorithms of the form

$$\mathbf{x}_k = P_{L_k}(\mathbf{y}_k), \quad (18)$$

$$\mathbf{y}_{k+1} = \mathbf{x}_k + \frac{t_k - 1}{t_{k+1}} (\mathbf{x}_k - \mathbf{x}_{k-1}) + \frac{t_k}{t_{k+1}} (\eta_k - 1) (\mathbf{x}_k - \mathbf{y}_k). \quad (19)$$

Under suitable conditions on the sequence $\{\eta_k\} \subset \mathbb{R}$, convergence can be proven to follow

$$\Psi(\mathbf{x}_k) - \Psi(\mathbf{x}^*) \leq \frac{2L_k \|\mathbf{x}_0 - \mathbf{x}^*\|^2}{\eta_k (k+1)^2}. \quad (20)$$

Notice that for $\eta_k = 2$ the \mathbf{y}_k update in (19) is the same than the one of OGM and the above convergence bound also equals the one for OGM. It appears not to be

possible, however, to prove convergence of algorithm (18)-(19) with $\eta_k \equiv 2$ for every problem [23]. Instead, in our approach a valid range of values for the coefficient η_k is computed during the execution of iteration k of the algorithm, but we noticed that in practice the upper bound of this range is often larger than 2, allowing, for example, us to often use $\eta_k \approx 2$ and thus to make (19) approximately equal to (14).

A similar method is the generalization of FISTA called OMFISTA [25]. The convergence theory provided for OMFISTA was valid only in the range $\eta_k \in (0, 1]$, and so did not include the case $\eta_k = 2$ that characterizes OISTA. In [28], monotone FISTA with variable acceleration (MFISTA-VA) is proposed, and it is shown that an $\eta_k > 2$ may be chosen when the new iterate \mathbf{x}_k satisfies $\Psi(\mathbf{x}_k) < \Psi(P_{L_k}(\mathbf{y}_k))$, which may lead to an extra algorithmic step and variable acceleration. Here we generalize what is proposed in [28] and prove that similar bounds can be achieved when (18) is used, thereby making our results relevant to the convergence of OISTA.

All of the above approaches speed up the Iterative Soft Thresholding Algorithm (ISTA), which has iterations of the form $\mathbf{x}_{k+1} = P_L(\mathbf{x}_k)$, using a momentum term that considers previous iterates when updating the current iterate. Another such approach, based on a different insight than Nesterov's, is the Two-Step Iterative Soft Thresholding (TwIST) [4] method. TwIST can be applied to problems of the form

$$\min \quad \frac{1}{2} \|K\mathbf{x} - \mathbf{b}\|^2 + \phi(\mathbf{x}) \quad (21)$$

and is considerably faster than IST in the case of poorly conditioned invertible operators K . TwIST is inspired by a two-step method for the solution of the linear system of equations $K\mathbf{x} = \mathbf{b}$ and is obtained by replacing appearances of a scaled version of the gradient ∇f of $f(\mathbf{x}) = \frac{1}{2} \|K\mathbf{x} - \mathbf{b}\|^2$ in that algorithm by the proximal-gradient operator P_L .

SpaRSA (Sparse Reconstruction by Separable Approximation) [24] is another approach for improving over IST. In this case, the smooth part f of problem (1) is not assumed to be convex and the key ingredient for the algorithm's efficiency seems to be a nonmonotone line-search procedure inspired by the seminal approach by Grippo, Lampariello and Lucidi (GLL) [11]. One interesting question regarding SpaRSA is whether the GLL line search could be replaced in SpaRSA by the nonmonotone line search of Zhang and Hager (ZH) [26], which in many cases compares favorably to GLL and whether these benefits of ZH would carry over to SpaRSA.

Yet another approach for generalizing and improving IST is the Generalized Iterative Shrinkage and Thresholding (GIST) algorithm [10]. The theory behind GIST convergence results removes the convexity hypothesis over f and relax that over ϕ in (1) by supposing instead that ϕ can be written as a difference of two convex functions. This latter assumption generalizes considerably over the convexity hypothesis usually imposed to the non-smooth part in IST-inspired methods while retaining important theoretical tools such as the existence of subderivatives and, consequently, the existence of useful necessary optimality conditions for this function.

3 The New Methods

In the current section we present our proposed algorithms in detail. We start by describing an abstract method, which we name Non-Deterministic PGM (NDPGM).

Algorithm 1 NDPGM

```

1: input  $t_1 \geq 1, \mathbf{y}_1 \in \mathbb{R}^n, N \in \mathbb{N}$ 
2: for  $k = 1, \dots, N$ 
3:   set  $L_k \in \mathbb{R}^n$ 
4:   set  $\mathbf{z}_k = P_{L_k}(\mathbf{y}_k)$ 
5:   set  $\mathbf{x}_k \in \mathbb{R}^n$ 
6:   set  $\eta_k \in \mathbb{R}$ 
7:   set  $t_{k+1} = \frac{1 + \sqrt{1 + 4t_k^2}}{2}$ 
8:   set  $\mathbf{y}_{k+1} = \mathbf{x}_k + \frac{t_k - 1}{t_{k+1}}(\mathbf{x}_k - \mathbf{x}_{k-1}) + \frac{t_k}{t_{k+1}}(\mathbf{z}_k - \mathbf{x}_k) + \frac{t_k}{t_{k+1}}(\eta_k - 1)(\mathbf{z}_k - \mathbf{y}_k)$ 

```

Note the non-deterministic nature of Steps 3, 5 and 6 of NDPGM. This leaves some important sequences unspecified, including the sequence of iterates $\{\mathbf{x}_k\} \subset \mathbb{R}^n$ itself. This is done on purpose so that NDPGM is a model for several methods. As two examples, notice how both FISTA [2] and MFISTA [3], described respectively in Algorithm 2 and Algorithm 3, fit this description. In both cases $\eta_k \equiv 1$ is used and a backtracking procedure is performed at Steps 5 and 6 of both algorithms in order to determine the parameter L_k at each iteration, measuring the difference between the function value $\Psi(P_{L_k}(\mathbf{y}_k))$ and $Q_{L_k}(P_{L_k}(\mathbf{y}_k), \mathbf{y}_k)$ where, for $L \in \mathbb{R}$ and $\mathbf{x}, \mathbf{y} \in \mathbb{R}^n$, $Q_L(\mathbf{x}, \mathbf{y})$ is the surrogate function:

$$Q_L(\mathbf{x}, \mathbf{y}) := f(\mathbf{y}) + \langle \nabla f(\mathbf{y}), \mathbf{x} - \mathbf{y} \rangle + \frac{L}{2} \|\mathbf{x} - \mathbf{y}\|^2 + \phi(\mathbf{x}). \quad (22)$$

The difference between these methods is that in FISTA we have $\mathbf{x}_k = \mathbf{z}_k$, while MFISTA uses $\mathbf{x}_k = \arg \min_{\mathbf{x} \in \{\mathbf{z}_k, \mathbf{x}_{k-1}\}} \Psi(\mathbf{x})$. The MFISTA-VA of [28] is also an instance of Algorithm 1, in this case with $\eta_k \geq 1$.

Algorithm 2 FISTA

```

1: input  $L_0 > 0, \beta > 1, \mathbf{x}_0 \in \mathbb{R}^n, N \in \mathbb{N}$ 
2: set  $t_1 = 1, \mathbf{y}_1 = \mathbf{x}_0$ 
3: for  $k = 1, \dots, N$ 
4:   set  $L_k = L_{k-1}$ 
5:   while  $\Psi(P_{L_k}(\mathbf{y}_k)) > Q_{L_k}(P_{L_k}(\mathbf{y}_k), \mathbf{y}_k)$ 
6:     set  $L_k = \beta L_k$ 
7:   set  $\mathbf{x}_k = P_{L_k}(\mathbf{y}_k)$ 
8:   set  $t_{k+1} = \frac{1 + \sqrt{1 + 4t_k^2}}{2}$ 
9:   set  $\mathbf{y}_{k+1} = \mathbf{x}_k + \frac{t_k - 1}{t_{k+1}}(\mathbf{x}_k - \mathbf{x}_{k-1})$ 

```

Before presenting our methods, we define the following:

$$\begin{aligned}
\Delta_a(L, \mathbf{y}) &:= Q_L(P_L(\mathbf{y}), \mathbf{y}) - \Psi(P_L(\mathbf{y})) \\
\Delta_b(\mathbf{x}, \mathbf{y}) &:= f(\mathbf{x}) - f(\mathbf{y}) - \langle \nabla f(\mathbf{y}), \mathbf{x} - \mathbf{y} \rangle \\
\Delta_c(L, \mathbf{x}, \mathbf{y}) &:= \phi(\mathbf{x}) - \phi(P_L(\mathbf{y})) - \langle -\nabla f(\mathbf{y}) - L(P_L(\mathbf{y}) - \mathbf{y}), \mathbf{x} - P_L(\mathbf{y}) \rangle.
\end{aligned} \quad (23)$$

Our proposed Fast Proximal Gradient Method (FPGM) is described in Algorithm 4.

Notice how the computation of $\Delta_a(L_k, \mathbf{y}_k)$, $\Delta_b(\mathbf{x}_{k-1}, \mathbf{y}_k)$, and $\Delta_c(L_k, \mathbf{x}_{k-1}, \mathbf{y}_k)$ uses only gradients and function evaluations that would have already been computed during the execution of the algorithm, except for the ϕ -values in $\Delta_c(L_k, \mathbf{x}_{k-1}, \mathbf{y}_k)$.

Algorithm 3 MFISTA

```

1: input  $L_0 > 0, \beta > 1, \mathbf{x}_0 \in \mathbb{R}^n, N \in \mathbb{N}$ 
2: set  $t_1 = 1, \mathbf{y}_1 = \mathbf{x}_0$ 
3: for  $k = 1, \dots, N$ 
4:   set  $L_k = L_{k-1}$ 
5:   while  $\Psi(P_{L_k}(\mathbf{y}_k)) > Q_{L_k}(P_{L_k}(\mathbf{y}_k), \mathbf{y}_k)$ 
6:     set  $L_k = \beta L_k$ 
7:   set  $\mathbf{z}_k = P_{L_k}(\mathbf{y}_k)$ 
8:   set  $\mathbf{x}_k = \arg \min_{\mathbf{x} \in \{\mathbf{z}_k, \mathbf{x}_{k-1}\}} \Psi(\mathbf{x})$ 
9:   set  $t_{k+1} = \frac{1 + \sqrt{1 + 4t_k^2}}{2}$ 
10:  set  $\mathbf{y}_{k+1} = \mathbf{x}_k + \frac{t_k - 1}{t_{k+1}}(\mathbf{x}_k - \mathbf{x}_{k-1}) + \frac{t_k}{t_{k+1}}(\mathbf{z}_k - \mathbf{x}_k)$ 

```

Algorithm 4 FPGM

```

1: input  $t_1 \geq 1, L_0 > 0, \beta > 1, \mathbf{x}_0 \in \mathbb{R}^n, K \in \mathbb{N}, \bar{\eta} \in [1, \infty) \cap \infty, N \in \mathbb{N}$ 
2: set  $\eta_0 = \bar{\eta}$ 
3: set  $\mathbf{y}_1 = \mathbf{x}_0$ 
4: for  $k = 1, \dots, N$ 
5:   set  $L_k = L_{k-1}$ 
6:   while  $\Psi(P_{L_k}(\mathbf{y}_k)) > Q_{L_k}(P_{L_k}(\mathbf{y}_k), \mathbf{y}_k)$ 
7:     set  $L_k = \beta L_k$ 
8:   set  $\mathbf{x}_k = P_{L_k}(\mathbf{y}_k)$ 
9:   set  $\gamma_k = 1 + 2 \frac{\Delta_a(L_k, \mathbf{y}_k) + (1 - 1/t_k)(\Delta_b(\mathbf{x}_{k-1}, \mathbf{y}_k) + \Delta_c(L_k, \mathbf{x}_{k-1}, \mathbf{y}_k))}{L_k \|\mathbf{z}_k - \mathbf{y}_k\|^2}$ 
10:  if  $k \leq K$ 
11:    set  $\eta_k = \min\{\gamma_k, \bar{\eta}\}$ 
12:  else
13:    set  $\eta_k = \min\{\gamma_k, \eta_{k-1} L_k / L_{k-1}, \bar{\eta}\}$ 
14:  set  $t_{k+1} = \frac{1 + \sqrt{1 + 4t_k^2}}{2}$ 
15:  set  $\mathbf{y}_{k+1} = \mathbf{x}_k + \frac{t_k - 1}{t_{k+1}}(\mathbf{x}_k - \mathbf{x}_{k-1}) + \frac{t_k}{t_{k+1}}(\eta_k - 1)(\mathbf{x}_k - \mathbf{y}_k)$ 

```

If this is costly, the user may simply replace $\Delta_c(L_k, \mathbf{x}_{k-1}, \mathbf{y}_k)$ computation by zero because $\Delta_c(L, \mathbf{x}, \mathbf{y}) \geq 0$, according to (28) in the next section, and the value used for η_k in Step 13 of Algorithm 4 is an upper bound for the valid range of values for η_k that ensure convergence, but smaller values can also be used. The monotone version of the FPGM, called MFPGM is given in Algorithm 5. The monotone versions of the FOMs have not to date been analyzed through the algorithm optimization approach of [6, 18] and the theory for these methods is known from the analysis of the more general monotone proximal gradient algorithms.

4 Convergence Analysis

We start with an introductory lemma, which will be repeatedly used in the remaining of the convergence analysis.

Lemma 1 *Let $\mathbf{x}, \mathbf{y} \in \mathbb{R}^n$, $\Psi : \mathbb{R}^n \rightarrow \mathbb{R}$ as in (1), $P_L : \mathbb{R}^n \rightarrow \mathbb{R}^n$ as in (3), and $0 < L \in \mathbb{R}$. Then*

$$\Psi(\mathbf{x}) - \Psi(P_L(\mathbf{y})) = \frac{L}{2} \|P_L(\mathbf{y}) - \mathbf{y}\|^2 + L \langle P_L(\mathbf{y}) - \mathbf{y}, \mathbf{y} - \mathbf{x} \rangle + \Delta(L, \mathbf{x}, \mathbf{y}) \quad (24)$$

Algorithm 5 MFBPGM

```

1: input  $t_1 \geq 1, L_0 > 0, \beta > 1, \mathbf{x}_0 \in \mathbb{R}^n, K \in \mathbb{N}, \bar{\eta} \in [1, \infty) \cap \infty, N \in \mathbb{N}$ 
2: set  $\eta_0 = \bar{\eta}$ 
3: set  $\mathbf{y}_1 = \mathbf{x}_0$ 
4: for  $k = 1, \dots, N$ 
5:   set  $L_k = L_{k-1}$ 
6:   while  $\Psi(P_{L_k}(\mathbf{y}_k)) > Q_{L_k}(P_{L_k}(\mathbf{y}_k), \mathbf{y}_k)$ 
7:     set  $L_k = \beta L_k$ 
8:   set  $\mathbf{z}_k = P_{L_k}(\mathbf{y}_k)$ 
9:   set  $\mathbf{x}_k = \arg \min_{\mathbf{x} \in \{\mathbf{z}_k, \mathbf{x}_{k-1}\}} \Psi(\mathbf{x})$ 
10:  set  $\gamma_k = 1 + 2 \frac{\Delta_a(L_k, \mathbf{y}_k) + (1 - 1/t_k)(\Delta_b(\mathbf{x}_{k-1}, \mathbf{y}_k) + \Delta_c(L_k, \mathbf{x}_{k-1}, \mathbf{y}_k)) + (\Psi(\mathbf{z}_k) - \Psi(\mathbf{x}_k))}{L_k \|\mathbf{z}_k - \mathbf{y}_k\|^2}$ 
11:  if  $k \leq K$ 
12:    set  $\eta_k = \min\{\gamma_k, \bar{\eta}\}$ 
13:  else
14:    set  $\eta_k = \min\{\gamma_k, \eta_{k-1} L_k / L_{k-1}, \bar{\eta}\}$ 
15:  set  $t_{k+1} = \frac{1 + \sqrt{1 + 4t_k^2}}{2}$ 
16:  set  $\mathbf{y}_{k+1} = \mathbf{x}_k + \frac{t_k - 1}{t_{k+1}}(\mathbf{x}_k - \mathbf{x}_{k-1}) + \frac{t_k}{t_{k+1}}(\mathbf{z}_k - \mathbf{x}_k) + \frac{t_k}{t_{k+1}}(\eta_k - 1)(\mathbf{z}_k - \mathbf{y}_k)$ 

```

with

$$\Delta(L, \mathbf{x}, \mathbf{y}) := \Delta_a(L, \mathbf{y}) + \Delta_b(\mathbf{x}, \mathbf{y}) + \Delta_c(L, \mathbf{x}, \mathbf{y}), \quad (25)$$

where $\Delta_a(L, \mathbf{y})$, $\Delta_b(\mathbf{x}, \mathbf{y})$, and $\Delta_c(L, \mathbf{x}, \mathbf{y})$ are defined in (23).

Proof Notice that, because of (22) and the first definition in (23), we have

$$\Psi(P_L(\mathbf{y})) = f(\mathbf{y}) + \langle \nabla f(\mathbf{y}), P_L(\mathbf{y}) - \mathbf{y} \rangle + \frac{L}{2} \|P_L(\mathbf{y}) - \mathbf{y}\|^2 + \phi(P_L(\mathbf{y})) - \Delta_a(L, \mathbf{y}), \quad (26)$$

Therefore,

$$\begin{aligned} \Psi(P_L(\mathbf{y})) &= f(\mathbf{x}) + \langle \nabla f(\mathbf{y}) + \phi'(P_L(\mathbf{y})), P_L(\mathbf{y}) - \mathbf{x} \rangle + \frac{L}{2} \|P_L(\mathbf{y}) - \mathbf{y}\|^2 + \\ &\quad \phi(\mathbf{x}) - \Delta_a(L, \mathbf{y}) - \Delta_b(\mathbf{x}, \mathbf{y}) - \\ &\quad (\phi(\mathbf{x}) - \phi(P_L(\mathbf{y})) - \langle \phi'(P_L(\mathbf{y})), \mathbf{x} - P_L(\mathbf{y}) \rangle), \end{aligned} \quad (27)$$

where $\phi'(P_L(\mathbf{y})) = -L(P_L(\mathbf{y}) - \mathbf{y}) - \nabla f(\mathbf{y})$ is a subgradient of ϕ at $P_L(\mathbf{y})$ according to the necessary and sufficient optimality conditions for (3) (we refer the reader to [16] for the definition and properties of a subgradient of a convex function, and also for optimality conditions for unconstrained convex minimization problems). Then

$$0 \leq \phi(\mathbf{x}) - \phi(P_L(\mathbf{y})) - \langle \phi'(P_L(\mathbf{y})), \mathbf{x} - P_L(\mathbf{y}) \rangle = \Delta_c(L, \mathbf{x}, \mathbf{y}) \quad (28)$$

and we have

$$\begin{aligned} \Psi(P_L(\mathbf{y})) &= f(\mathbf{x}) + \langle \nabla f(\mathbf{y}) + \phi'(P_L(\mathbf{y})), P_L(\mathbf{y}) - \mathbf{x} \rangle + \frac{L}{2} \|P_L(\mathbf{y}) - \mathbf{y}\|^2 + \\ &\quad \phi(\mathbf{x}) - \Delta_a(L, \mathbf{y}) - \Delta_b(\mathbf{x}, \mathbf{y}) - \Delta_c(L, \mathbf{x}, \mathbf{y}). \end{aligned} \quad (29)$$

Rearranging we get

$$\Psi(\mathbf{x}) - \Psi(P_L(\mathbf{y})) = \langle L(P_L(\mathbf{y}) - \mathbf{y}), P_L(\mathbf{y}) - \mathbf{x} \rangle - \frac{L}{2} \|P_L(\mathbf{y}) - \mathbf{y}\|^2 + \Delta(L, \mathbf{x}, \mathbf{y}), \quad (30)$$

and then

$$\Psi(\mathbf{x}) - \Psi(P_L(\mathbf{y})) = L \langle P_L(\mathbf{y}) - \mathbf{y}, \mathbf{y} - \mathbf{x} \rangle + \frac{L}{2} \|P_L(\mathbf{y}) - \mathbf{y}\|^2 + \Delta(L, \mathbf{x}, \mathbf{y}). \quad (31)$$

The next result is our main convergence theorem. It will be proven under the general condition (32) on the parameters L_k and η_k . This condition may involve the optimal point and is likely not verifiable in practice. Later we will show how to guarantee validity of (32) through more concrete conditions that can be verified in a practical setting.

Theorem 1 Fix $\mathbf{x}^* \in \mathbb{R}^n$ and let $\Delta(L, \mathbf{x}, \mathbf{y})$ be as in (25), then Algorithm 1 under conditions

$$(\eta_k - 1)t_k^2 \|\mathbf{z}_k - \mathbf{y}_k\|^2 \leq \frac{2}{L_k} \left(t_k(t_k - 1)\Delta(L_k, \mathbf{x}_{k-1}, \mathbf{y}_k) + t_k\Delta(L_k, \mathbf{x}^*, \mathbf{y}_k) + t_k^2(\Psi(\mathbf{z}_k) - \Psi(\mathbf{x}_k)) \right) \quad (32)$$

or, equivalently,

$$\eta_k \leq 1 + \frac{2}{L_k \|\mathbf{z}_k - \mathbf{y}_k\|^2} \left((1 - 1/t_k)\Delta(L_k, \mathbf{x}_{k-1}, \mathbf{y}_k) + (1/t_k)\Delta(L_k, \mathbf{x}^*, \mathbf{y}_k) + (\Psi(\mathbf{z}_k) - \Psi(\mathbf{x}_k)) \right) \quad (33)$$

and

$$\frac{\eta_{k+1}}{L_{k+1}} \leq \frac{\eta_k}{L_k} \quad (34)$$

satisfies

$$\begin{aligned} \Psi(\mathbf{x}_k) - \Psi(\mathbf{x}^*) &\leq \\ &\frac{2L_k}{\eta_k (k + 2t_1 - 1)^2} \left(\frac{2\eta_1 t_1^2 (\Psi(\mathbf{x}_1) - \Psi(\mathbf{x}^*))}{L_1} + \right. \\ &\quad \left. \|\eta_1 t_1 (\mathbf{z}_1 - \mathbf{y}_1) + t_1 \mathbf{y}_1 - (t_1 - 1)\mathbf{x}_0 - \mathbf{x}^*\|^2 \right). \quad (35) \end{aligned}$$

Proof Using Lemma 1 with $L = L_{k+1}$, $\mathbf{x} = \mathbf{x}_k$, and $\mathbf{y} = \mathbf{y}_{k+1}$, we obtain, because $\mathbf{z}_{k+1} = P_{L_{k+1}}(\mathbf{y}_{k+1})$,

$$\begin{aligned} \Psi(\mathbf{x}_k) - \Psi(\mathbf{x}_{k+1}) &= \Psi(\mathbf{x}_k) - \Psi(\mathbf{z}_{k+1}) + (\Psi(\mathbf{z}_{k+1}) - \Psi(\mathbf{x}_{k+1})) \\ &= \frac{L_{k+1}}{2} \|\mathbf{z}_{k+1} - \mathbf{y}_{k+1}\|^2 + \\ &\quad L_{k+1} \langle \mathbf{z}_{k+1} - \mathbf{y}_{k+1}, \mathbf{y}_{k+1} - \mathbf{x}_k \rangle + \\ &\quad \Delta(L_{k+1}, \mathbf{x}_k, \mathbf{y}_{k+1}) + (\Psi(\mathbf{z}_{k+1}) - \Psi(\mathbf{x}_{k+1})). \quad (36) \end{aligned}$$

Therefore,

$$\begin{aligned} \frac{2}{L_{k+1}} (d_k - d_{k+1}) &= \|\mathbf{z}_{k+1} - \mathbf{y}_{k+1}\|^2 + 2 \langle \mathbf{z}_{k+1} - \mathbf{y}_{k+1}, \mathbf{y}_{k+1} - \mathbf{x}_k \rangle + \\ &\quad \frac{2}{L_{k+1}} \left(\Delta(L_{k+1}, \mathbf{x}_k, \mathbf{y}_{k+1}) + (\Psi(\mathbf{z}_{k+1}) - \Psi(\mathbf{x}_{k+1})) \right), \quad (37) \end{aligned}$$

where $d_k = \Psi(\mathbf{x}_k) - \Psi(\mathbf{x}^*)$. Using Lemma 1 once more in the same manner, but now with $\mathbf{x} = \mathbf{x}^*$, we have

$$\begin{aligned} \frac{2}{L_{k+1}} (-d_{k+1}) &= \|\mathbf{z}_{k+1} - \mathbf{y}_{k+1}\|^2 + 2 \langle \mathbf{z}_{k+1} - \mathbf{y}_{k+1}, \mathbf{y}_{k+1} - \mathbf{x}^* \rangle + \\ &\quad \frac{2}{L_{k+1}} \left(\Delta(L_{k+1}, \mathbf{x}^*, \mathbf{y}_{k+1}) + (\Psi(\mathbf{z}_{k+1}) - \Psi(\mathbf{x}_{k+1})) \right) \end{aligned} \quad (38)$$

Multiplying the above equations by $t_{k+1}(t_{k+1} - 1)$ and t_{k+1} , respectively, and adding the results we get

$$\begin{aligned} \frac{2}{L_{k+1}} \left(t_{k+1}(t_{k+1} - 1)d_k - t_{k+1}^2 d_{k+1} \right) &= t_{k+1}^2 \|\mathbf{z}_{k+1} - \mathbf{y}_{k+1}\|^2 + \\ &\quad 2 \langle t_{k+1}(\mathbf{z}_{k+1} - \mathbf{y}_{k+1}), t_{k+1}\mathbf{y}_{k+1} - (t_{k+1} - 1)\mathbf{x}_k - \mathbf{x}^* \rangle + \\ &\quad \frac{2}{L_{k+1}} \left(t_{k+1}(t_{k+1} - 1)\Delta(L_{k+1}, \mathbf{x}_k, \mathbf{y}_{k+1}) + \right. \\ &\quad \left. t_{k+1}\Delta(L_{k+1}, \mathbf{x}^*, \mathbf{y}_{k+1}) + t_{k+1}^2(\Psi(\mathbf{z}_{k+1}) - \Psi(\mathbf{x}_{k+1})) \right). \end{aligned} \quad (39)$$

Now we use the fact that the algorithm satisfies $t_{k+1}(t_{k+1} - 1) = t_k^2$, resulting in

$$\begin{aligned} \frac{2}{L_{k+1}} \left(t_k^2 d_k - t_{k+1}^2 d_{k+1} \right) &= t_{k+1}^2 \|\mathbf{z}_{k+1} - \mathbf{y}_{k+1}\|^2 + \\ &\quad 2 \langle t_{k+1}(\mathbf{z}_{k+1} - \mathbf{y}_{k+1}), t_{k+1}\mathbf{y}_{k+1} - (t_{k+1} - 1)\mathbf{x}_k - \mathbf{x}^* \rangle \\ &\quad + \frac{2}{L_{k+1}} \left(t_{k+1}(t_{k+1} - 1)\Delta(L_{k+1}, \mathbf{x}_k, \mathbf{y}_{k+1}) + \right. \\ &\quad \left. t_{k+1}\Delta(L_{k+1}, \mathbf{x}^*, \mathbf{y}_{k+1}) + t_{k+1}^2(\Psi(\mathbf{z}_{k+1}) - \Psi(\mathbf{x}_{k+1})) \right). \end{aligned} \quad (40)$$

Then we apply the relation

$$\langle \mathbf{x}, \mathbf{y} \rangle = \frac{1}{2\eta} (\|\eta\mathbf{x} + \mathbf{y}\|^2 - \|\eta\mathbf{x}\|^2 - \|\mathbf{y}\|^2) \quad (41)$$

to obtain

$$\begin{aligned} \frac{2}{L_{k+1}} \left(t_k^2 d_k - t_{k+1}^2 d_{k+1} \right) &= t_{k+1}^2 \|\mathbf{z}_{k+1} - \mathbf{y}_{k+1}\|^2 \\ &\quad + \frac{1}{\eta_{k+1}} \left\| \eta_{k+1} t_{k+1} (\mathbf{z}_{k+1} - \mathbf{y}_{k+1}) + t_{k+1}\mathbf{y}_{k+1} - (t_{k+1} - 1)\mathbf{x}_k - \mathbf{x}^* \right\|^2 \\ &\quad - \frac{1}{\eta_{k+1}} \|\eta_{k+1} t_{k+1} (\mathbf{z}_{k+1} - \mathbf{y}_{k+1})\|^2 - \frac{1}{\eta_{k+1}} \|t_{k+1}\mathbf{y}_{k+1} - (t_{k+1} - 1)\mathbf{x}_k - \mathbf{x}^*\|^2 \\ &\quad + \frac{2}{L_{k+1}} \left(t_{k+1}(t_{k+1} - 1)\Delta(L_{k+1}, \mathbf{x}_k, \mathbf{y}_{k+1}) + \right. \\ &\quad \left. t_{k+1}\Delta(L_{k+1}, \mathbf{x}^*, \mathbf{y}_{k+1}) + t_{k+1}^2(\Psi(\mathbf{z}_{k+1}) - \Psi(\mathbf{x}_{k+1})) \right). \end{aligned} \quad (42)$$

Let us then denote

$$\mathbf{u}_{k+1} := \eta_{k+1} t_{k+1} (\mathbf{z}_{k+1} - \mathbf{y}_{k+1}) + t_{k+1}\mathbf{y}_{k+1} - (t_{k+1} - 1)\mathbf{x}_k - \mathbf{x}^* \quad (43)$$

and notice that \mathbf{y}_{k+1} was defined in such a way that

$$\mathbf{u}_k = t_{k+1}\mathbf{y}_{k+1} - (t_{k+1} - 1)\mathbf{x}_k - \mathbf{x}^* \quad (44)$$

so that we can then rewrite (42) as

$$\begin{aligned} \frac{2}{L_{k+1}} \left(t_k^2 d_k - t_{k+1}^2 d_{k+1} \right) &= (1 - \eta_{k+1}) t_{k+1}^2 \|\mathbf{z}_{k+1} - \mathbf{y}_{k+1}\|^2 + \\ &\quad \frac{1}{\eta_{k+1}} \|\mathbf{u}_{k+1}\|^2 - \frac{1}{\eta_{k+1}} \|\mathbf{u}_k\|^2 \\ &\quad + \frac{2}{L_{k+1}} \left(t_{k+1} (t_{k+1} - 1) \Delta(L_{k+1}, \mathbf{x}_k, \mathbf{y}_{k+1}) + \right. \\ &\quad \left. t_{k+1} \Delta(L_{k+1}, \mathbf{x}^*, \mathbf{y}_{k+1}) + t_{k+1}^2 (\Psi(\mathbf{z}_{k+1}) - \Psi(\mathbf{x}_{k+1})) \right). \end{aligned} \quad (45)$$

Considering hypothesis (32) we have

$$\frac{2}{L_{k+1}} \left(t_k^2 d_k - t_{k+1}^2 d_{k+1} \right) \geq \frac{1}{\eta_{k+1}} \|\mathbf{u}_{k+1}\|^2 - \frac{1}{\eta_{k+1}} \|\mathbf{u}_k\|^2, \quad (46)$$

and then

$$\frac{2\eta_{k+1}}{L_{k+1}} \left(t_k^2 d_k - t_{k+1}^2 d_{k+1} \right) \geq \|\mathbf{u}_{k+1}\|^2 - \|\mathbf{u}_k\|^2. \quad (47)$$

Thus using the hypothesis $\eta_k/L_k \geq \eta_{k+1}/L_{k+1}$:

$$\frac{2\eta_k t_k^2 d_k}{L_k} - \frac{2\eta_{k+1} t_{k+1}^2 d_{k+1}}{L_{k+1}} \geq \|\mathbf{u}_{k+1}\|^2 - \|\mathbf{u}_k\|^2. \quad (48)$$

Notice that denoting the above inequality as $a_k - a_{k+1} \geq b_{k+1} - b_k$ we can rearrange to $a_{k+1} + b_{k+1} \leq a_k + b_k$ which, because the sequences $\{a_k\}$ and $\{b_k\}$ are non-negative, leads us to $a_k \leq a_1 + b_1$, that is,

$$\frac{2\eta_k t_k^2 d_k}{L_k} \leq \frac{2\eta_1 t_1^2 d_1}{L_1} + \|\mathbf{u}_1\|^2. \quad (49)$$

That is

$$\Psi(\mathbf{x}_k) - \Psi(\mathbf{x}^*) \leq \frac{L_k}{2\eta_k t_k^2} \left(\frac{2\eta_1 t_1^2 d_1}{L_1} + \|\mathbf{u}_1\|^2 \right). \quad (50)$$

By noticing that $t_k \geq (k + 2t_1 - 1)/2$ we get the desired result.

Now we discuss practical ways of ensuring that (32) holds. A first step towards doing so is to consider Beck and Teboulle's sufficient decrease criterion, which entails choosing at each iteration k of the algorithm a parameter L_k such that

$$\Psi(P_{L_k}(\mathbf{y}_k)) \leq Q_{L_k}(P_{L_k}(\mathbf{y}_k), \mathbf{y}_k). \quad (51)$$

If such a criterion is used, it is straightforward to notice that $\Delta(L_k, \mathbf{x}, \mathbf{y}_k)$ is larger than or equal 0 for every $\mathbf{x} \in \mathbb{R}^n$ and, therefore, for every $t_1 \geq 1$, condition (33) is guaranteed to hold with $\eta_k \equiv 1$, in which case we recover the original FISTA when using $\mathbf{x}_k = \mathbf{z}_k$, as in Algorithm 2, and MFISTA when using $\mathbf{x}_k = \arg \min_{\mathbf{x} \in \{\mathbf{z}_k, \mathbf{x}_{k-1}\}} \Psi(\mathbf{x})$, as in Algorithm 3. We are, however, interested in the case where η_k can be made considerably larger than 1, because it can yield faster convergence in practice.

The key difficulty in using condition (33) is that we would have to be able to compute $\Delta(L_k, \mathbf{x}^*, \mathbf{y}_k) = \Delta_a(L_k, \mathbf{y}_k) + \Delta_b(\mathbf{x}^*, \mathbf{y}_k) + \Delta_c(L_k, \mathbf{x}^*, \mathbf{y}_k)$ which would involve an unknown optimizer \mathbf{x}^* . However, from convexity of f and ϕ , we know that $\Delta_b(\mathbf{x}^*, \mathbf{y}_k) \geq 0$ and that $\Delta_c(L_k, \mathbf{x}^*, \mathbf{y}_k) \geq 0$. Therefore, the following verifiable condition is sufficient

$$\eta_k \leq 1 + \frac{2}{L_k \|\mathbf{z}_k - \mathbf{y}_k\|^2} \left(\Delta_a(L_k, \mathbf{y}_k) + (1 - 1/t_k) \left(\Delta_b(\mathbf{x}_{k-1}, \mathbf{y}_k) + \Delta_c(L_k, \mathbf{x}_{k-1}, \mathbf{y}_k) \right) + (\Psi(\mathbf{z}_k) - \Psi(\mathbf{x}_k)) \right). \quad (52)$$

We next prove the convergence of Algorithm 6 below, which is called General FPGM (GFPGM). The theoretical analysis uses hypotheses that allow the inclusion as special cases, for example, FPGM and its monotone version MFPGM, which are respectively Algorithms 4 and 5 above.

Algorithm 6 GFPGM

```

1: input  $t_1 \geq 1, L_0 > 0, \beta > 1, \mathbf{y}_1, \mathbf{x}_0 \in \mathbb{R}^n, K \in \mathbb{N}, \bar{\eta} \in [1, \infty) \cap \infty, N \in \mathbb{N}$ 
2: set  $\eta_0 = \bar{\eta}$ 
3: for  $k = 1, \dots, N$ 
4:   set  $L_k = L_{k-1}$ 
5:   while  $\Psi(P_{L_k}(\mathbf{y}_k)) > Q_{L_k}(P_{L_k}(\mathbf{y}_k), \mathbf{y}_k)$ 
6:     set  $L_k = \beta L_k$ 
7:   set  $\mathbf{z}_k = P_{L_k}(\mathbf{y}_k)$ 
8:   set  $\mathbf{x}_k \in \{\mathbf{x} : \Psi(\mathbf{x}) \leq \Psi(\mathbf{z}_k)\}$ 
9:   set  $\gamma_k = 1 + 2 \frac{\Delta_a(L_k, \mathbf{y}_k) + (1 - 1/t_k) (\Delta_b(\mathbf{x}_{k-1}, \mathbf{y}_k) + \Delta_c(L_k, \mathbf{x}_{k-1}, \mathbf{y}_k)) + (\Psi(\mathbf{z}_k) - \Psi(\mathbf{x}_k))}{L_k \|\mathbf{z}_k - \mathbf{y}_k\|^2}$ 
10:  if  $k \leq K$ 
11:    set  $\eta_k \in [1, \bar{\eta}]$ 
12:  else
13:    set  $\eta_k \leq \min\{\gamma_k, \eta_{k-1} L_k / L_{k-1}, \bar{\eta}\}$ 
14:  set  $t_{k+1} = \frac{1 + \sqrt{1 + 4t_k^2}}{2}$ 
15:  set  $\mathbf{y}_{k+1} = \mathbf{x}_k + \frac{t_k - 1}{t_{k+1}} (\mathbf{x}_k - \mathbf{x}_{k-1}) + \frac{t_k}{t_{k+1}} (\mathbf{z}_k - \mathbf{x}_k) + \frac{t_k}{t_{k+1}} (\eta_k - 1) (\mathbf{z}_k - \mathbf{y}_k)$ 

```

Corollary 1 Let $\{\mathbf{x}_k\} \subset \mathbb{R}^n$ be the sequence generated by Algorithm 6 with $K = 0$, $t_1 = 1$ and $\mathbf{y}_1 = \mathbf{x}_0$. Fix some $\mathbf{x}^* \in \mathbb{R}^n$. Then we have

$$\Psi(\mathbf{x}_k) - \Psi(\mathbf{x}^*) \leq \frac{2L_k \|\mathbf{x}_k - \mathbf{x}^*\|^2}{\eta_k (k+1)^2}. \quad (53)$$

Proof First we observe that the method indeed leaves Steps (5) and (6) of Algorithm 6. Let \mathcal{L} be the Lipschitz constant of ∇f . Then, as it is well known, for $L \geq \mathcal{L}$, the condition $Q_L(\mathbf{x}, \mathbf{y}) \geq \Psi(\mathbf{x})$ holds for every pair of vectors $\mathbf{x}, \mathbf{y} \in \mathbb{R}^n$. Therefore, at iteration k , the loop of Steps (5) and (6) of Algorithm 6 will be executed at most K_k times where $K_k = \left\lceil \frac{\log \frac{\mathcal{L}}{L_{k-1}}}{\log \beta} \right\rceil$, and where $\lceil x \rceil$ is the smaller integer larger than or equal x . In fact, $\max\{L_0, \beta \mathcal{L}\}$ is an upper bound to L_k .

Notice that Steps 9 and 13 of Algorithm 6 ensure that conditions (33) and (34) are satisfied, so that Theorem 1 can be applied in this case leading to

$$\Psi(\mathbf{x}_k) - \Psi(\mathbf{x}^*) \leq \frac{2L_k}{\eta_k(k+2t_1-1)^2} \left(\frac{2\eta_1 t_1^2 (\Psi(\mathbf{x}_1) - \Psi(\mathbf{x}^*))}{L_1} + \|\eta_1 t_1 (\mathbf{z}_1 - \mathbf{x}_0) + \mathbf{x}_0 - \mathbf{x}^*\|^2 \right). \quad (54)$$

Now, we use Lemma 1 with $L = L_1$, $\mathbf{x} = \mathbf{x}^*$, $\mathbf{y}_1 = \mathbf{x}_0$, and $\mathbf{y} = \mathbf{y}_1$ followed by (41) to obtain

$$\begin{aligned} \Psi(\mathbf{x}_1) - \Psi(\mathbf{x}^*) &= \Psi(\mathbf{z}_1) - \Psi(\mathbf{x}^*) + (\Psi(\mathbf{x}_1) - \Psi(\mathbf{z}_1)) \\ &= -\frac{L_1}{2} \|\mathbf{z}_1 - \mathbf{y}_1\|^2 - L_1 \langle \mathbf{z}_1 - \mathbf{y}_1, \mathbf{y}_1 - \mathbf{x}^* \rangle - \\ &\quad \Delta(L_1, \mathbf{x}^*, \mathbf{y}_1) + (\Psi(\mathbf{x}_1) - \Psi(\mathbf{z}_1)) \\ &= -\frac{L_1}{2} \|\mathbf{z}_1 - \mathbf{x}_0\|^2 - L_1 \langle \mathbf{z}_1 - \mathbf{x}_0, \mathbf{x}_0 - \mathbf{x}^* \rangle - \\ &\quad \Delta(L_1, \mathbf{x}^*, \mathbf{y}_1) + (\Psi(\mathbf{x}_1) - \Psi(\mathbf{z}_1)). \end{aligned} \quad (55)$$

On the other hand,

$$\begin{aligned} \langle \mathbf{z}_1 - \mathbf{x}_0, \mathbf{x}_0 - \mathbf{x}^* \rangle &= \frac{1}{2\eta_1 t_1} (\|\eta_1 t_1 (\mathbf{z}_1 - \mathbf{x}_0) + \mathbf{x}_0 - \mathbf{x}^*\|^2 - \\ &\quad \|\eta_1 t_1 (\mathbf{z}_1 - \mathbf{x}_0)\|^2 - \|\mathbf{x}_0 - \mathbf{x}^*\|^2). \end{aligned} \quad (56)$$

Thus

$$\begin{aligned} \frac{2\eta_1 t_1^2 (\Psi(\mathbf{x}_1) - \Psi(\mathbf{x}^*))}{L_1} &= -\eta_1 t_1^2 \|\mathbf{z}_1 - \mathbf{x}_0\|^2 - t_1 \|\eta_1 t_1 (\mathbf{z}_1 - \mathbf{x}_0) + \mathbf{x}_0 - \mathbf{x}^*\|^2 + \\ &\quad t_1 \|\eta_1 t_1 (\mathbf{z}_1 - \mathbf{x}_0)\|^2 + t_1 \|\mathbf{x}_0 - \mathbf{x}^*\|^2 + \\ &\quad \frac{2\eta_1 t_1^2}{L_1} (\Delta(L_1, \mathbf{x}^*, \mathbf{y}_1) + (\Psi(\mathbf{x}_1) - \Psi(\mathbf{z}_1))) \\ &= -\eta_1 t_1^2 \|\mathbf{z}_1 - \mathbf{x}_0\|^2 \left(1 - \eta_1 t_1 - \right. \\ &\quad \left. \frac{2(\Delta(L_1, \mathbf{x}^*, \mathbf{y}_1) + (\Psi(\mathbf{x}_1) - \Psi(\mathbf{z}_1)))}{L_1 \|\mathbf{z}_1 - \mathbf{x}_0\|^2} \right) - \\ &\quad t_1 \|\eta_1 t_1 (\mathbf{z}_1 - \mathbf{x}_0) + \mathbf{x}_0 - \mathbf{x}^*\|^2 + \\ &\quad t_1 \|\mathbf{x}_0 - \mathbf{x}^*\|^2. \end{aligned} \quad (57)$$

We simplify the result adopting the notation

$$\epsilon_1 := 1 - \eta_1 t_1 - \frac{2(\Delta(L_1, \mathbf{x}^*, \mathbf{y}_1) + (\Psi(\mathbf{x}_1) - \Psi(\mathbf{z}_1)))}{L_1 \|\mathbf{z}_1 - \mathbf{x}_0\|^2} \quad (59)$$

finally reaching

$$\begin{aligned} \frac{2\eta_1 t_1^2 (\Psi(\mathbf{x}_1) - \Psi(\mathbf{x}^*))}{L_1} &+ \|\eta_1 t_1 (\mathbf{z}_1 - \mathbf{x}_0) + \mathbf{x}_0 - \mathbf{x}^*\|^2 = \\ &- \eta_1 t_1^2 \epsilon_1 \|\mathbf{z}_1 - \mathbf{x}_0\|^2 + (1 - t_1) \|\eta_1 t_1 (\mathbf{z}_1 - \mathbf{x}_0) + \mathbf{x}_0 - \mathbf{x}^*\|^2 + t_1 \|\mathbf{x}_0 - \mathbf{x}^*\|^2. \end{aligned} \quad (60)$$

Now, notice that with $t_1 = 1$, Steps 9 and 13 of Algorithm 6 will ensure $\epsilon_1 \geq 0$ and, therefore,

$$\frac{2\eta_1 t_1^2 (\Psi(\mathbf{x}_1) - \Psi(\mathbf{x}^*))}{L_1} + \|\eta_1 t_1 (\mathbf{z}_1 - \mathbf{x}_0) + \mathbf{x}_0 - \mathbf{x}^*\|^2 \leq \|\mathbf{x}_0 - \mathbf{x}^*\|^2. \quad (61)$$

This put into (54) gives the desired result.

The main intent of the previous corollary is to ease the comparison of bound (35) of Theorem 1 with current knowledge about fast proximal gradient methods. It shows that indeed, if it is possible to use $\eta_k \equiv 2$ in OISTA, this algorithm will share the same bound on the objective function gap that has OGM and that $\eta_k > 2$ may lead to an even better constant in the convergence bound. Unfortunately, if $t_1 = 1$, it is possible to show that $\eta_1 \leq 2$, and it can be seen that $\eta_1 = 2$ is very unlikely to happen. In fact, η_1 can be constrained this way to be no larger than 1 if $\mathbf{x}_1 = \mathbf{z}_1$ and $Q_{L_1}(\mathbf{z}_1, \mathbf{y}_1) = \Psi(\mathbf{z}_1)$. Then, if, as it is commonly the case, the step parameter L_k never changes, we will permanently have to use $\eta_k < 2$. On the other hand, this is not an issue with $K > 0$. Furthermore, $O(1/k^2)$ convergence for Algorithm 6 is still valid for $K > 0$. This is so because although Theorem 1 cannot be applied to Algorithm 6 with $K > 0$, one can still apply Theorem 1 to Algorithm 6 with $K = 0$, but now restarted with $L_0 = L_K$, $\mathbf{y}_1 = \mathbf{y}_{K+1}$, $t_1 = t_{K+1}$, and $\mathbf{x}_0 = \mathbf{x}_K$.

5 Experiments

We will divide the experimental section in two parts. The first of these parts deals with high-resolution synchrotron-illuminated tomographic image reconstruction of a biological sample. In this first part we compare several fast proximal gradient algorithms from the viewpoint of amount of objective function value reduction per computational time in order to capture an idea of the relative algorithm performances regarding numerical optimization speed.

Objective function value alone is not a measure of quality of image reconstruction. This is why in the second set of experiments we use simulated data from known mathematical images in order to compare the reconstructions against a ground truth, which did not exist in the previous case of the reconstruction of biological samples. The comparisons use realistic task-oriented numerical figures of merit. These experiments are repeated and statistical hypothesis testing is used in order to assess the relevance of the outcome.

Before heading to the experimental details, we explain generalities of the tomographic image reconstruction problem. In tomography, the goal is to reconstruct an image $\rho : \mathbb{R}^2 \rightarrow \mathbb{R}$ from a finite number of approximate samples of its Radon transform $\mathcal{R}[\rho] : [0, \pi) \times \mathbb{R} \rightarrow \mathbb{R}$, which is defined as

$$\mathcal{R}[\rho](\theta, t) := \int_{-\infty}^{\infty} \rho \left(t \begin{pmatrix} \cos \theta \\ \sin \theta \end{pmatrix} + s \begin{pmatrix} -\sin \theta \\ \cos \theta \end{pmatrix} \right) ds, \quad (62)$$

see Figure 1 for an illustration. Assuming that the image belongs to a linear space spanned by a basis $\{\rho_1, \rho_2, \dots, \rho_n\}$ and because there is a finite number of samples $b_i \approx \mathcal{R}[\rho](\theta_i, t_i)$, $i \in \{1, 2, \dots, m\}$, the problem is then reduced to a linear system of equations

$$R\mathbf{x} \approx \mathbf{b}, \quad (63)$$

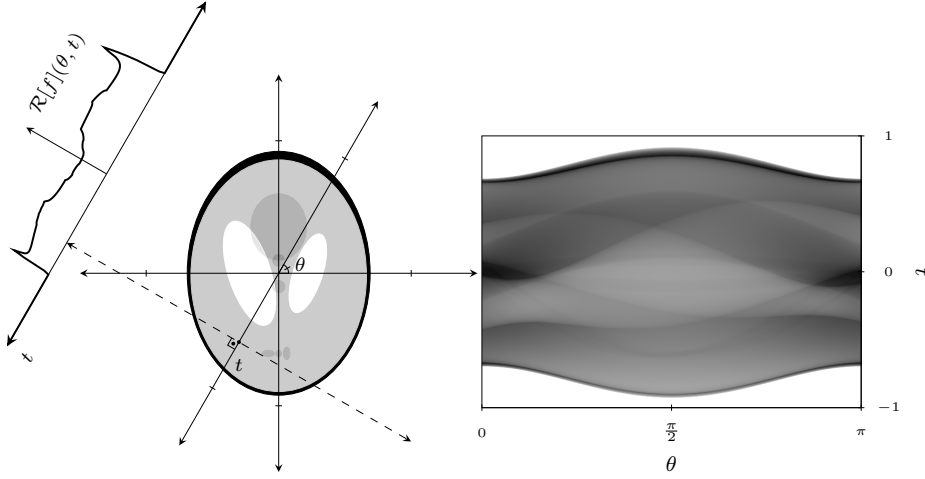


Fig. 1 Left: integration path for the Radon transform. There, θ is the angle between the normal to the integration path and the horizontal axis, and t is the distance from the line of integration to the origin. Right: gray-scale image in the $\theta \times t$ coordinate system of the Radon transform of the image shown on the left.

where the unknowns $\mathbf{x} \in \mathbb{R}^n$ are the coefficients of the linear combination that gives the reconstruction $\rho_{\text{recon}} := \sum_{j=1}^n x_j \rho_j$. In practice the meaning of the approximation above has to be made clear, which can be done by, e.g., optimization. In this setting, the constrained least squares

$$\mathbf{x} \in \arg \min_{\mathbf{y} \in \mathbb{R}_+^n} \|\mathbf{R}\mathbf{y} - \mathbf{b}\|^2, \quad (64)$$

is one among the many possible models. Because the tomographic reconstruction problem is poorly conditioned, regularization is commonly applied and the situation can in many cases be interpreted as the minimization of the sum of a smooth convex function f and a non-smooth convex function ϕ as in (1), the problem which fast proximal gradient methods are designed to solve. In theory, because the Radon transform is a compact linear operator, its inverse is (moderately) ill-posed [7]. In practice, this ill-posedness can be problematic in some circumstances. For example, in acquisitions where the signal to noise ratio is below ideal such as when lower exposure to radiation is desired or when the source is less predictable such as in emission tomography. Beyond these cases, there might be reasons that make a shorter acquisition time necessary (for example, for 4D tomography), which might amplify the ill-posedness of the problem because higher scanning speeds are usually obtained by sampling radially at a lower rate.

5.1 Constrained Maximum Likelihood Tomography with Synchrotron Data

In synchrotron tomography, $\mathcal{R}[\rho](\theta_i, t_i)$ can be estimated by a computation involving d_i , ω_i , and p_i , where

- d_i is a measurement of the dark field, which is the expected number of detected events in the sensor during a scan without active source and without the object between source and detector;

- ω_i is a measurement of the flat field, which is the expected number of detected events in the sensor during a scan with active source and without the object between source and detector;
- p_i is the photon count, i.e., the number of events in the sensor during a scan with active source and with the object between source and detector.

Another idea is, instead of estimating $\mathcal{R}[\rho](\theta_i, t_i)$ from dark field, flat field, and photon count data, to use the probabilistically inspired constrained model for transmission data from [8], which we describe now. Let

$$f(\mathbf{x}) = \sum_{i=1}^m h_i((R\mathbf{x})_i), \quad (65)$$

where

$$h_i(b) = \omega_i e^{-b} + d_i - p_i \log(\omega_i e^{-b} + d_i). \quad (66)$$

Thus, the model consists of solving

$$\min_{\mathbf{x} \in \mathbb{R}_+^n} f(\mathbf{x}), \quad (67)$$

which is equivalent to

$$\min_{\mathbf{x} \in \mathbb{R}^n} f(\mathbf{x}) + \phi(\mathbf{x}), \quad (68)$$

where $\phi(\mathbf{x}) = \chi_{\mathbb{R}_+^n}(\mathbf{x})$, with the indicator function χ_C of a convex closed set C defined as

$$\chi_C(\mathbf{x}) = \begin{cases} 0 & \text{if } \mathbf{x} \in C \\ \infty & \text{otherwise.} \end{cases} \quad (69)$$

The proximal operator of the indicator function is the Euclidean projection:

$$\text{prox}_{\chi_C}(\mathbf{x}) = \mathcal{P}_C(\mathbf{x}) = \arg \min_{\mathbf{y} \in C} \|\mathbf{x} - \mathbf{y}\|. \quad (70)$$

Data Geometry and Dimensions Data was collected along $m_r = 2048$ parallel lines on each one of the $m_v = 512$ views and the path between emitter and detector for data point i was parametrized by the pair (θ_i, t_i) for $i \in \{1, 2, \dots, m_r m_v\}$ in the following manner. First let us define $\kappa_i \in \{1, 2, \dots, m_v\}$ as $\kappa_i := 1 + \lfloor (i-1)/m_r \rfloor$ where $\lfloor x \rfloor$ is the largest integer smaller than or equal x and $\ell_i \in \{1, 2, \dots, m_r\}$ as $\ell_i := 1 + (i-1) \% m_r$ where $a \% b$ is the remainder of the integer division of $a \in \mathbb{N}$ by $b \in \mathbb{N}$. Then, for $i \in \{1, 2, \dots, m_r m_v\}$, we have

$$\theta_i = -\pi \frac{(\kappa_i - 1)}{m_v - 1} \quad \text{and} \quad t_i = -1 + 2 \frac{(\ell_i - 1)}{m_r - 1}. \quad (71)$$

The dimensions of the reconstructed images are $n = 2048^2$, that is, 2048×2048 pixels.

In the transmission tomography setup found at the Brazilian Synchrotron Light Laboratory, the object to be imaged is positioned between the synchrotron x-ray source and a scintillator that is digitally imaged by a CCD camera. Data from the κ -th readout from this camera provides a 2048×2048 radio-graphic image that includes the photon counts at pixels of the camera corresponding to integration lines with parameters $\theta = -\pi(\kappa - 1)/(m_v - 1)$ and $t \in \left\{ -1 + 2 \frac{(\ell-1)}{m_r-1} : \ell \in \{1, 2, \dots, m_r\} \right\}$ not only for one two-dimensional slice, but simultaneously for 2048 parallel slices of the imaged volume. Reconstruction of each of the slices is later performed independently through the two-dimensional model. Figure 2 depicts the procedure used to obtain the photon count data p_i that will be used for one slice reconstruction.

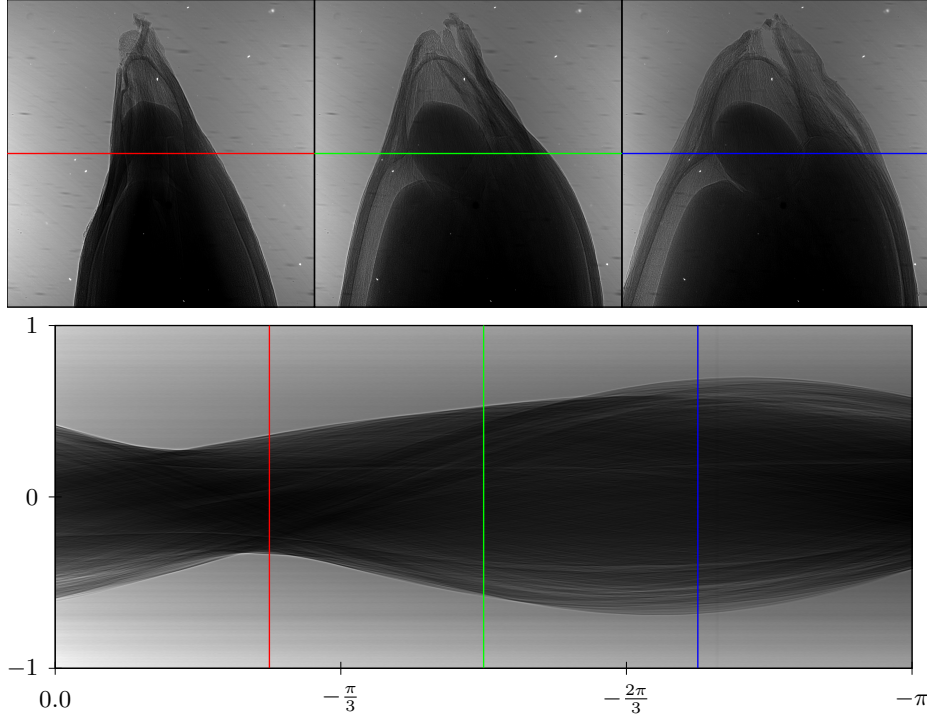


Fig. 2 Top: three of the 512 images used in the reconstruction of a slice of an apple seed. These images depict the number of photons recorded on each sensor pixel, where brighter indicates more photons recorded. The solid lines indicate data corresponding to the slice that will be reconstructed in the experiments. Bottom: photon count data that will be used for the reconstruction of the slice. Each of the 512 rows of the data related to the same slice is used as a column in a representation of the data as samples of the photon counts in the $\theta \times t$ plane. The color of each of the solid lines identifies the position where the corresponding data in the top row was used.

Algorithm 7 OISTA

```

1: input  $L_0 > 0, \beta > 1, \mathbf{x}_0 \in \mathbb{R}^n, N \in \mathbb{N}$ 
2: set  $t_1 = 1, \mathbf{y}_1 = \mathbf{x}_0$ 
3: for  $k = 1, \dots, N$ 
4:   set  $L_k = L_{k-1}$ 
5:   while  $\Psi(P_{L_k}(\mathbf{y}_k)) > Q_{L_k}(P_{L_k}(\mathbf{y}_k), \mathbf{y}_k)$ 
6:     set  $L_k = \beta L_k$ 
7:   set  $\mathbf{x}_k = P_{L_k}(\mathbf{y}_k)$ 
8:   set  $t_{k+1} = \frac{1 + \sqrt{1 + 4t_k^2}}{2}$ 
9:   set  $\mathbf{y}_{k+1} = \mathbf{x}_k + \frac{t_k - 1}{t_{k+1}}(\mathbf{x}_k - \mathbf{x}_{k-1}) + \frac{t_k}{t_{k+1}}(\mathbf{x}_k - \mathbf{y}_k)$ 

```

Algorithms We have compared several algorithms regarding speed of reduction of objective function value. The methods experimented with are the following: FISTA (Algorithm 2) and OISTA (Algorithm 7), which we compare against FPGM (Algorithm 4). In every case, the starting image \mathbf{x}_0 was set to an image such that all of its pixels have the same value and $\sum_{i=1}^m (R\mathbf{x}_0)_i = \sum_{i=1}^m \tilde{b}_i$, where \tilde{b}_i are the estimates of the Radon

Transform given by $\tilde{b}_i = \ln \frac{\omega_i - d_i}{p_i - d_i}$. The parameter β was set to 2 for all algorithms. This seemed a reasonable choice and we did not feel the need to experiment with this parameter. A first comparison uses $K = 10$ and $\bar{\eta} = \infty$ for FPGM and compares it to FISTA and OISTA. A second experiment considers only FPGM, but with three different set of parameters K and $\bar{\eta}$, namely $(K, \bar{\eta}) \in \{(10, \infty), (10, 2), (\infty, \infty)\}$. We denote the FPGM variations as $\text{FPGM}_{(K, \bar{\eta})}$ with $(K, \bar{\eta}) \in \{(10, \infty), (10, 2), (\infty, \infty)\}$. The reason why the value $\bar{\eta} = 2$ was singled out among all the possible finite values for this parameter is that when $\eta_k = 2$ the FPGM iteration is identical to the one of OISTA, for which no convergence proof exists. This way we show that our theoretical results can explain why OISTA converges in some cases, while at the same time they give insights on when and why OISTA might not converge. Notice that the theoretical results presented above do not guarantee convergence of $\text{FPGM}_{(\infty, \infty)}$ because it may not satisfy (34). In fact, Figure 5 shows what seems to be an example of the algorithm not converging to an optimizer.

Computational Issues Because of the large data and image size, the matrix-vector products $R\mathbf{x}$ and $R^T\mathbf{b}$ were implemented in a parallel fashion and the computations were carried out by a Graphics Processing Unit (GPU) using C++ CUDA in order to obtain low running times for the reconstruction and thus to enable experimentation with a wide range of parameters and for a very large number of iterations. A Python wrapper for the GPU routines was used in order to implement all the other algorithm parts using the NumPy library. We have used the ray-tracing method from [12] for the on-the-fly computation of these matrix-vector products. All other computations were accomplished by the CPU. The computer had a GeForce Titan Xp GPU with 12GB of dedicated RAM and a Ryzen 5 2600 CPU with 16GB of available RAM. The algorithms are also practical when executed in less powerful hardware, as Figure 4 shows. In practice far less than 1000 iterations will be executed and the algorithm will be executed with a single set of parameters, which means that even modest CPUs such as the one used suffice for routine reconstruction. The single precision GPU implementation runs at around 12 times faster than the double precision CPU implementation.

Discussion We base our discussion on log-plots of the objective function reduction as iterations proceed. In these plots we represent the evolution of the relative difference between the object function value obtained by each algorithm and the value obtained by FISTA after 2000 iterations (using $1/L_0 = 1.3 \cdot 10^{-4}$). We denote the reference image obtained by this long run of FISTA by $\tilde{\mathbf{x}}$. The starting stepsize for the long FISTA run was selected in order to obtain good convergence and running FISTA for twice as many iterations as the other methods ensured that the final iterations obtained this way by FISTA had better objective function value than the other methods.

For a comparison of FPGM with existing algorithms, we have tested the behavior of $\text{FPGM}_{(10, \infty)}$ and compared it to FISTA and OISTA. We notice in Figure 3 that $\text{FPGM}_{(10, \infty)}$ is very competitive regardless of the starting stepsize adopted within the experimented range. We have tried running the algorithm for a variety of stepsizes within the range $1/L_0 \in [9 \cdot 10^{-5}, 2 \cdot 10^{-4}]$. This range was chosen because it contains the value of $1/L_{1000}$ obtained by the line search procedure if values above this range were used. This means that smaller stepsize values unnecessarily slow down the algorithms and should not be used, whereas for larger values the line search reduces the stepsize in the first few iterations to something within the adopted range. For the sake of legibility, we present the results obtained for only two values of $1/L_0$ showing the typical

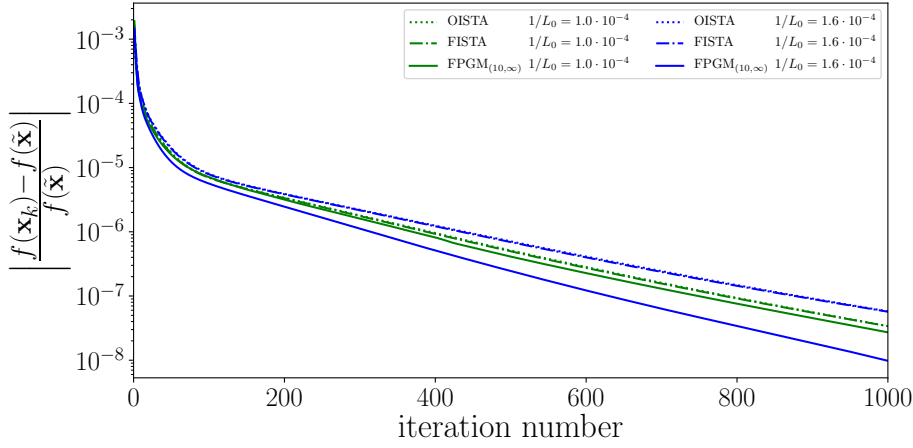


Fig. 3 Plot of objective function value at each iteration for two different starting step-size values in three different algorithms.

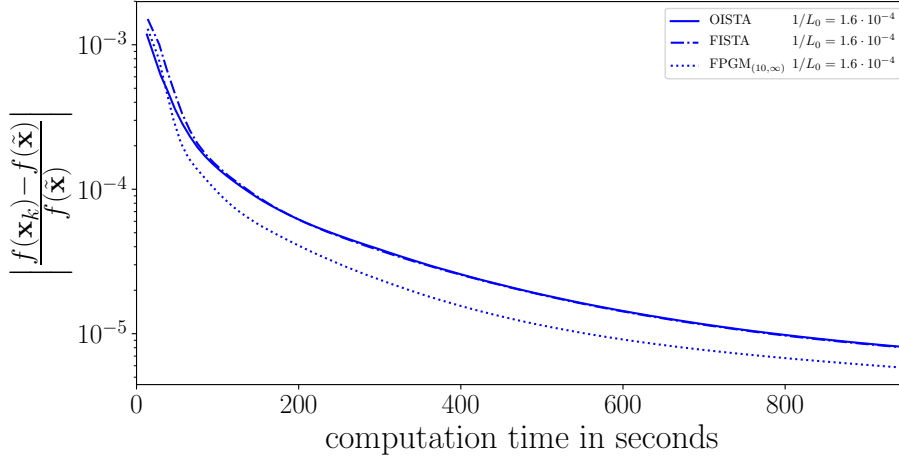


Fig. 4 Plot of objective function over time in three different algorithms, running on the CPU.

behavior. We note that, for a favorable selection of starting stepsize FPGM outperforms noticeably the other methods, whereas for some values of the starting stepsize the improvements may be small.

Figure 5 illustrates an experiment designed to investigate sensitivity of Algorithm 4 to the choice of parameters K and $\bar{\eta}$. As it can be seen, at least for this combination of optimization model and data, $\text{FPGM}_{(10, \infty)}$ and $\text{FPGM}_{(10, 2)}$, which are provably convergent, appear to have advantages over $\text{FPGM}_{(\infty, \infty)}$, which does not necessarily satisfy (34) and, therefore, has no proven convergence. Also, it seems that limiting the value of η_k does not necessarily reduce convergence speed when all other parameters are the same. Convergent versions of FPGM did not present any drastic performance changes within the set of parameters used, which is a sign of robustness with relation to parameter selection.

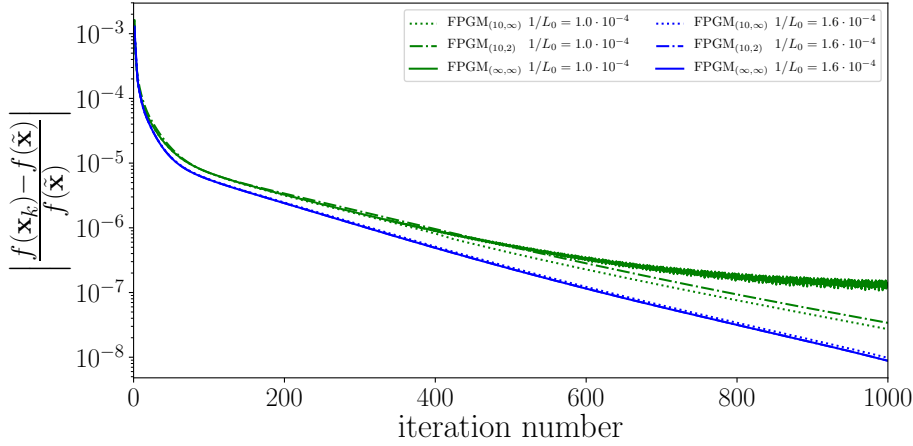


Fig. 5 Comparison of the behavior of the objective function value of the iterates of $\text{FPGM}_{(K,\bar{\eta})}$ for some values of parameters K , $\bar{\eta}$, and L_0 . Notice that because $\text{FPGM}_{(\infty,\infty)}$ might not converge, oscillatory behavior is observed for some starting stepsize values.

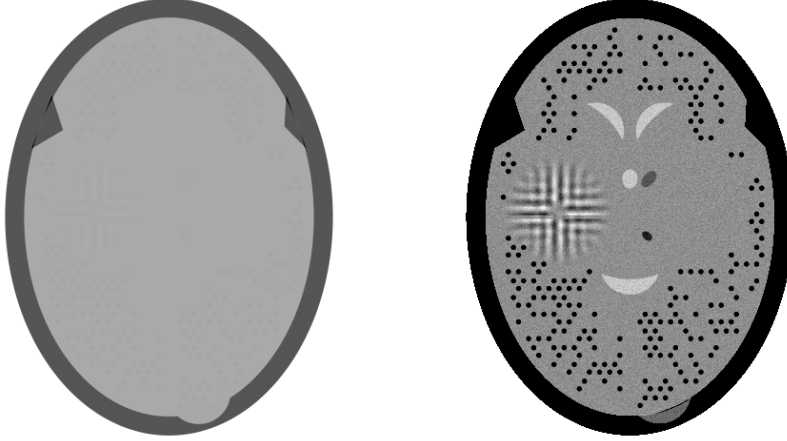


Fig. 6 One of the possible phantoms used in the statistical hypothesis testing experiment. On the left, the full range of attenuation values of the phantom is shown, its minimum value represented as white and the maximum as black. On the right, values below 0.204 cm^{-1} are shown as white and values above 0.21765 cm^{-1} are shown as black.

5.2 Reconstruction from Simulated Data

In the present subsection we perform reconstruction from simulated data in order to be able to measure reconstruction quality. We have performed several similar experiments with the intention of performing statistical testing on the hypothesis that one algorithm performs better than the other with respect to a well defined mathematical figure of merit. We will first describe how each reconstruction experiment was performed and then we discuss the results of the statistical hypothesis testing.

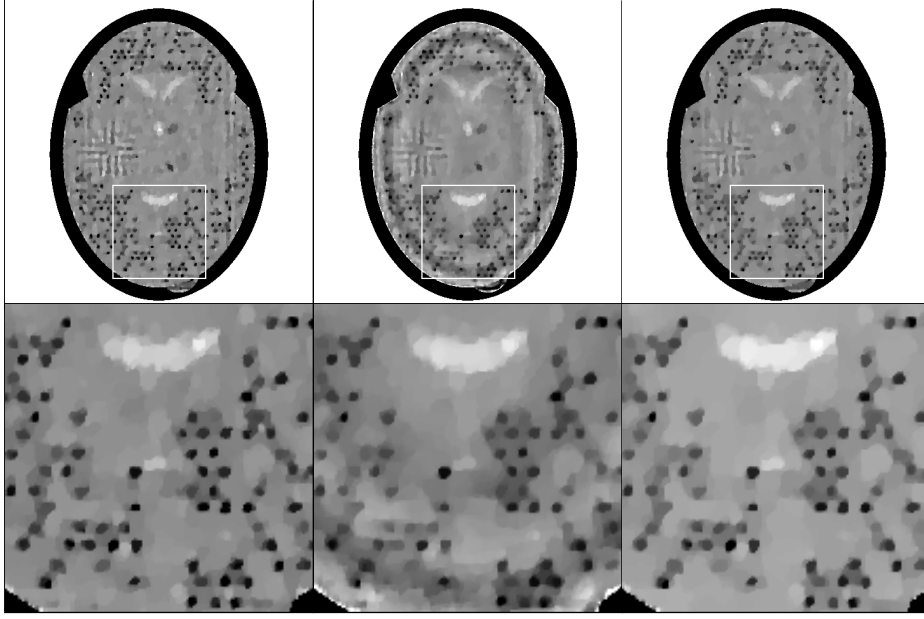


Fig. 7 Left: First iteration of SupART to reach stopping criterion. Center: 50th iteration of $\text{FPGM}_{(10,\infty)}^{5 \cdot 10^{-3}}$. Right: 100th iteration of $\text{FPGM}_{(10,\infty)}^{5 \cdot 10^{-3}}$. Top: full images. Bottom: details for easier inspection.

Test Images and Projection Data Each reconstruction experiment was based on a mathematical phantom defined from simple geometrical features, which can be seen in Figure 6. It has a skull-like high-attenuation feature around it, while possessing less contrasting objects inside the skull. Among the features inside the skull there are small similar circular objects scattered inside the inner structure. The number of such objects is constant, but its position vary on each experiment in the following form: each object must exist in a position or else to exist in the same position except that mirrored along the central vertical axis. The side where the circular object will be placed is selected at random with equal probability of selection for left and right placement. The other features of the phantom do not change from one experiment to another, except for a small random inhomogeneity, which may also be different from one experiment to another. Generation of the images, simulation of tomographic data from each generated image, and reconstruction from each of the simulated dataset was automatically handled by the "experimenter" feature of SNARK14 software.¹ For this set of experiments, the sequential implementations provided by SNARK14 were used instead of the specially crafted parallel algorithms used in the previous set of experiments.

For these experiments, data acquisition followed a divergent beam geometry where detectors are distributed in a circular strip centered at the X-ray source with source-to-origin distance (that is, the radius of the source's circular path followed during acquisition) equal to 78 cm and with source-to-detector distance (that is, the radius of the circular strip of detectors) equal to 110.735 cm. The simulated circular detector

¹ SNARK14 may be downloaded free of charge from <http://turing.iimas.unam.mx/SNARK14M/>

strip contained 693 detectors with the spacing between the center of successive detectors equal to 0.0533 cm. Each projection contains data from all 693 detectors and 180 of such projections were measured, 2° apart from each other. Reconstructed images had 485×485 pixels covering the square $[-9.1 \text{ cm}, 9.1 \text{ cm}]^2$.

Reconstruction Model In these experiments, for the reconstruction with FPGM we used the least squares model with Total Variation regularization. Let us first define the Total Variation as

$$TV(\mathbf{x}) := \sum_{i=1}^m \sqrt{(x_i - x_{r(i)})^2 + (x_i - x_{a(i)})^2}, \quad (72)$$

where $r(i)$ is the index of the pixel to the right of pixel i and $a(i)$ is the index of the pixel above pixel i . The Total Variation regularization functional was chosen because of its computational convenience and good regularization properties for tomographic images.

Our model therefore is

$$\min_{\mathbf{x} \in \mathbb{R}_+^n} \|R\mathbf{x} - \mathbf{b}\|^2 + \lambda TV(\mathbf{x}), \quad (73)$$

where $R \in \mathbb{R}^{m \times n}$ is the matrix representing the discretization of the Radon Transform and $\mathbf{b} \in \mathbb{R}^m$ contains the simulated data. This model can be rewritten as

$$\min_{\mathbf{x} \in \mathbb{R}^n} f(\mathbf{x}) + \phi(\mathbf{x}), \quad (74)$$

where $f(\mathbf{x}) = \|R\mathbf{x} - \mathbf{b}\|^2$ and $\phi(\mathbf{x}) = \lambda TV(\mathbf{x}) + \chi_{\mathbb{R}_+^n}(\mathbf{x})$. The proximal operator for $\phi(\mathbf{x}) = \lambda TV(\mathbf{x}) + \chi_{\mathbb{R}_+^n}(\mathbf{x})$ was approximately computed by 10 steps of the fast gradient method for the dual formulation of the constrained TV proximal problem, according to [3].

ART One of the tested algorithms is FPGM_(10,∞), as described above. The other is a superiorized version of the Algebraic Reconstruction Technique (ART). ART is a common denomination for a series of algorithms that sequentially update the reconstructed image using one row of the system $R\mathbf{x} = \mathbf{b}$ (where \mathbf{b} is the tomographic data and R is the projection matrix) at a time. The meaning of "superiorized" will be explained after we describe ART itself. The precise version of ART used here is described as Algorithm 8 below, where \mathbf{r}_i is the i -th row of the matrix R (an n -dimensional row-vector).

Algorithm 8 ART

```

1: input  $\alpha \in \mathbb{R}, \{i_0, i_1, \dots, i_{m-1}\} \subset \mathbb{N}, \mathbf{x} \in \mathbb{R}^n, \mathbf{b} \in \mathbb{R}^m$ 
2: set  $\mathbf{y}_0 = \mathbf{x}$ 
3: for  $\ell = 0, \dots, m-1$ 
4:   set  $\mathbf{y}_{\ell+1} = \mathbf{y}_\ell - \alpha \frac{\langle \mathbf{r}_{i_\ell}^T, \mathbf{y}_\ell \rangle - \mathbf{b}_{i_\ell}}{\|\mathbf{r}_{i_\ell}^T\|^2} \mathbf{r}_{i_\ell}^T$ 
5: return  $\mathbf{y}_m$ 

```

We will denote the result of the application of Algorithm 8 to a given $\mathbf{x} \in \mathbb{R}^n$ as $\text{ART}(\mathbf{x})$, omitting the other input parameters that will be kept fixed as follows: $\alpha =$

0.05, which is known as the relaxation parameter, $\mathbf{b} \in \mathbb{R}^m$ which is the tomographic data, and the sequence $\{i_0, i_1, \dots, i_{m-1}\}$, that determines the order of processing of the tomographic data within the full cycle of Algorithm 8, which is defined according to the "efficient" sequence described in [14]. This sequence was shown experimentally to improve convergence of the method.

Superiorization Superiorization is a technique for the modification of iterative optimization (or feasibility) algorithms that possess resiliency to summable perturbations. It consists of replacing the iteration \mathbf{x}_k of a given algorithm by a perturbed version $\tilde{\mathbf{x}}_k$ prior to applying the computations that will lead to the next iteration \mathbf{x}_{k+1} of the method. The perturbations, which we may denote as $\mathbf{s}_k := \tilde{\mathbf{x}}_k - \mathbf{x}_k$, are usually designed to improve the iterates according to a secondary criterion represented by a function $\phi : \mathbb{R}^n \rightarrow \mathbb{R}$. By an improvement we mean a reduction of the value of ϕ , that is, \mathbf{s}_k is normally designed so that $\phi(\mathbf{x}_k + \mathbf{s}_k) \leq \phi(\mathbf{x}_k)$. In our experiments we have used $\phi = TV$, i.e., the Total Variation defined in (72) is the secondary criterion for superiorization.

Algorithm 9 describes the procedure that we use to superiorize ART in our experiments. It makes use of the concept of non-ascending vectors. We define the set $\tilde{\partial}\phi(\mathbf{x})$ of non-ascending vectors for a convex function $\phi : \mathbb{R}^n \rightarrow \mathbb{R}$ from a point $\mathbf{x} \in \mathbb{R}^n$ as the set of vectors $\mathbf{t} \in \mathbb{R}^n$ with $\|\mathbf{t}\| \leq 1$ and such that there is $B > 0$ for which $b \in [0, B]$ implies that $\phi(\mathbf{x} + b\mathbf{t}) \leq \phi(\mathbf{x})$. Notice that $\mathbf{0} \in \tilde{\partial}\phi(\mathbf{x})$, meaning that the set of non-ascending vectors is never empty. Following [15, Theorem 2], we can construct a non-ascending vector \mathbf{t} for ϕ from \mathbf{x} as follows, first componentwise defining an auxiliary vector $\tilde{\mathbf{t}} \in \mathbb{R}^n$ as

$$\tilde{t}_i = \begin{cases} \frac{\partial\phi}{\partial x_i}(\mathbf{x}) & \text{if } \frac{\partial\phi}{\partial x_i}(\mathbf{x}) \text{ is well defined} \\ 0 & \text{otherwise,} \end{cases} \quad \text{and then defining} \quad \mathbf{t} = \begin{cases} -\frac{\tilde{\mathbf{t}}}{\|\tilde{\mathbf{t}}\|} & \text{if } \tilde{\mathbf{t}} \neq \mathbf{0} \\ \mathbf{0} & \text{otherwise.} \end{cases} \quad (75)$$

We will denote the output of Algorithm 9 for given $\mathbf{x} \in \mathbb{R}^n$ and $l \in \mathbb{N}$ as $\text{SupTV}(\mathbf{x}, l)$, omitting parameters a, b and I , which were kept fixed with the values $a = 1 - 10^{-4}$, $b = 3 \cdot 10^{-2}$, and $I = 10$.

Algorithm 9 SupTV

```

1: input  $\mathbf{x} \in \mathbb{R}^n, l \in \mathbb{N}, a \in (0, 1), b \in (0, \infty), I \in \mathbb{N}$ 
2: set  $\mathbf{y} = \mathbf{x}$ 
3: for  $i = 1, 2, \dots, I$ 
4:   set  $\mathbf{t} \in \tilde{\partial}TV(\mathbf{y})$ 
5:   do
6:     set  $\tilde{b} = ba^l$ 
7:     set  $\tilde{\mathbf{y}} = \mathbf{y} + \tilde{b}\mathbf{t}$ 
8:     set  $l = l + 1$ 
9:   while  $TV(\tilde{\mathbf{y}}) > TV(\mathbf{y})$ 
10:  set  $\mathbf{y} = \tilde{\mathbf{y}}$ 
11: return  $(\mathbf{y}, l)$ 
```

It is important to notice that superiorization according to the criterion ϕ does not mean minimization of that criterion. This makes the approach much more flexible than optimization because the theory is easier to develop for a large variety of secondary

criteria. On the other hand, it is clear that, because there is no guarantee of minimization, there may exist images that are equally data-consistent than those obtained by superiorization, but that are better according to ϕ . In practice, however, superiorized methods have been shown to be almost as fast as the non-superiorized version of the same method, to be very flexible and simple to use in practice, and to deliver considerably improved results when compared to its non-superiorized counterpart.

Algorithm 10 SupART

```

1: input  $\mathbf{x}_0 \in \mathbb{R}^n$ ,  $\epsilon \in \mathbb{R}$ ,  $\mathbf{b} \in \mathbb{R}^m$ 
2: set  $l_0 = 0$ ,  $k = 0$ 
3: while  $\|R\mathbf{x}_k - \mathbf{b}\|^2 > \epsilon$ 
4:   set  $(\mathbf{x}_{k+1/2}, l_{k+1}) = \text{SupTV}(\mathbf{x}_k, l_k)$ 
5:   set  $\mathbf{x}_{k+1} = \text{ART}(\mathbf{x}_{k+1/2})$ 
6:   set  $k = k + 1$ 
7: return  $\mathbf{x}_k$ 

```

SupART We can finally precisely define the algorithm that we have compared to FPGM in the experiments described in the present subsection. Each iteration of Superiorized ART (SupART), presented in Algorithm 10, is defined as application of Algorithm 9 followed by application of Algorithm 8. Unlike FPGM which uses a prescribed number of iterations, our version of SupART uses a stopping criterion based in data-fidelity, as measured by the squared residual $\|R\mathbf{x} - \mathbf{b}\|^2$. We have done so in order to force the images obtained by SupART to have a data-fidelity value that is similar to those obtained by FPGM. We will describe precisely how it was done below, when discussing the parameter selection for the algorithms and models.

Parameter Selection Algorithm $\text{FPGM}_{(10,\infty)}$ was used with parameters $L_0 = 1$, $\beta = 2$, and $N = 100$ in order to solve model (73). In this case we are not comparing convergence speed between variations of the same algorithm, so the choice of parameters is not critical and these values work well in practice. For the model to be fully defined, the value of regularization parameter λ has to be specified. We now describe how we have decided which values to use for λ : We have generated a phantom and simulated tomographic data from this phantom as described above, and then ran the method for the set of parameters $\lambda \in \{10^{-4}, 5 \cdot 10^{-4}, 10^{-3}, 5 \cdot 10^{-3}, 10^{-2}, 5 \cdot 10^{-2}\}$. We verified that, among these, the value $\lambda = 5 \cdot 10^{-3}$ provided the highest value of the Imagewise Region of Interest (IROI) figure of merit (the IROI is precisely described below, see (76)). Then, we have selected two other values for the regularization parameter within the same order of magnitude, leading to the final set of regularization parameters that were used in the final algorithmic comparison: $\lambda \in \{4, 5, 6\} \cdot 10^{-3}$.

SupART has already been tested for this reconstruction problem in [9], and we have used the (already mentioned above) same set of parameters as in that reference ($\alpha = 0.05$, $a = 1 - 10^{-4}$, $b = 3 \cdot 10^{-2}$) with one exception. In [9] the authors have used $I = 40$, while we have used $I = 10$ in order to match the number of the iterations used by the approximation algorithm for the proximal operator of the TV that is used in FPGM. SupART also requires the determination of the stopping parameter ϵ , which we have selected to be 2.33 because this is, up to three digits accuracy, what $\text{FPGM}_{(10,\infty)}$ obtained after 100 iterations when solving (73) with $\lambda = 5 \cdot 10^{-3}$.

Finally, both FPGM and SupART require the selection of a starting image \mathbf{x}_0 , which we have selected to be a uniform image such that $\sum_{i=1}^m (R\mathbf{x}_0)_i = \sum_{i=1}^m b_i$.

Image Reconstruction Evaluation Comparison of the tested algorithms was done according to the IROI figure of merit. The IROI is defined in [19] and we provide a succinct explanation of it here. The IROI considers only paired structures, which in our case were each of the small circles (tumors) in the phantom shown at Figure 6 and its empty counterpart on the other side of the phantom. We associate each of these pairs of structures with an index ranging from 1 to S . Let, for $s \in \{1, 2, \dots, S\}$, $\alpha_t^p(s)$ be the average density in the phantom on the region where the tumor s is present, and $\alpha_n^p(s)$ be the average density in the phantom on the respective region where the tumor s is not present. Similarly, $\alpha_t^r(s)$ and $\alpha_n^r(s)$ are the average values of these regions in the reconstructed images. Then, the value of the IROI is given by

$$\frac{\sum_{s=1}^S (\alpha_t^r(s) - \alpha_n^r(s))}{\sum_{s=1}^S \left(\alpha_n^r(s) - \frac{1}{S} \sum_{s'=1}^S \alpha_n^r(s') \right)^2} / \frac{\sum_{s=1}^S (\alpha_t^p(s) - \alpha_n^p(s))}{\sum_{s=1}^S \left(\alpha_n^p(s) - \frac{1}{S} \sum_{s'=1}^S \alpha_n^p(s') \right)^2}. \quad (76)$$

Large IROI values mean that we have large differences $\alpha_t^r(s) - \alpha_n^r(s)$ and, therefore, that reconstructed images with large IROI values tend to offer easier detectability of the tumors in the regions of interest than images with low IROI.

The last sentence indicates the essential nature of IROI; its purpose is to measure the efficacy of an algorithm for tumor detectability in the reconstructions. It is different from measures based on the overall similarity between the phantoms and their reconstructions, such as structural similarity (SSIM). Those other measures are likely to indicate better the perceived quality of the whole reconstruction, but IROI is more useful for evaluating the diagnostic efficacy of a reconstruction algorithm for the specific task of tumor detection [19].

Discussion We have performed 30 repetitions of the cycle of **(i)** generating a random phantom, **(ii)** simulating projection data from the phantom, **(iii)** reconstructing images from the simulated data with SupART and FPGM (for the three versions of model (73) with $\lambda \in \{4, 5, 6\} \cdot 10^{-3}$), and **(iv)** computing the IROI of the reconstructed images. These 30 repetitions were used for statistical testing of the null hypothesis (H_0) "SupART reconstructs an image with IROI equally large as the one obtained by $\text{FPGM}_{(10,\infty)}^\lambda$ ", where $\text{FPGM}_{(10,\infty)}^\lambda$ denotes $\text{FPGM}_{(10,\infty)}$ applied to the solution of (73) with regularization parameter λ . The results can be seen on Table 1, where we have denoted the estimated likelihood of rejecting H_0 while it is true by P_0 .

Figure 7 shows reconstructions obtained by SupART and $\text{FPGM}_{(10,\infty)}^{5 \cdot 10^{-3}}$ in the last of the 30 experiments for an illustration of the difference of the results of the algorithms. We remark that although FPGM is a fast algorithm, certain features take a large number of iterations to be accurately captured by the method. Notice how a low-frequency low-contrast artifact in the form of radial waves can be seen in the 50th iteration of $\text{FPGM}_{(10,\infty)}$. This artifact is not present if the algorithm is allowed to run for more time. This is not a feature exclusively present in FPGM nor it is exclusive to the particular selection of algorithmic parameters that were used in our experiments, but rather a common issue with all the fast proximal gradient methods which might not have been noticed before because low-contrast features such as those in the phantom we

Algorithm	Mean IROI	P_0
$\text{FPGM}_{(10,\infty)}^{4 \cdot 10^{-3}}$	0.1914	$3.093 \cdot 10^{-8}$
$\text{FPGM}_{(10,\infty)}^{5 \cdot 10^{-3}}$	0.1883	$3.437 \cdot 10^{-8}$
$\text{FPGM}_{(10,\infty)}^{6 \cdot 10^{-3}}$	0.1623	$1.342 \cdot 10^{-7}$
SupART	0.1438	N/A

Table 1 Mean IROIs (larger is better) and estimated probabilities of rejecting a true null hypothesis.

use are not usually investigated in simulated reconstructions. Indeed, even Conjugate Gradient methods seem to present such kind of artifact (see, e.g., Figure 4(b) in [27]).

Although it can be seen that in this particular setting the FPGM reconstructions are consistently better than SupART reconstructions, we make no claims that FPGM performs better than SupART in general because the experiments were performed for a particular set of simulation and algorithmic parameters. It was not our intent to optimize SupART’s parameter for this specific reconstruction problem, but it may well be the case that SupART could obtain results as good (or better) as those obtained by FPGM if the parameters were more carefully adjusted for the particular problem at hand. However, the experiments allow us to conclude that FPGM is competitive with state-of-the-art methods in terms of image quality reconstruction.

6 Conclusions and Future Work

We have introduced a new algorithm called FPGM with convergence rate $O(1/k^2)$ for the minimization of a separable smooth plus nonsmooth convex function. The convergence theory we have developed for this algorithm explains why OISTA [18] converges in many circumstances even though in the worst-case scenario OISTA is non-convergent [23]. In large-scale experiments with real world data, FPGM consistently outperforms, from the viewpoint of objective function reduction, FISTA, and in many cases FPGM performs better than OISTA in practice. Experiments performed from simulated data showed that FPGM presents reconstructed images of good quality, but it was noticed that a large number of iterations may be required in order to eliminate low-contrast artifacts that are present in the early iterations of the algorithm. In future research on this subject we plan to investigate the causes of such artifacts and to devise ways of avoiding them occurring in the early iterates [1].

Acknowledgments

This study has support by NIH grants R01-AR060238, R01-AR067156, and R01-AR068966, and was performed under the rubric of the Center of Advanced Imaging Innovation and Research (CAI²R), a NIBIB Biomedical Technology Resource Center (NIH P41-EB017183). E. S. Helou was partially supported by FAPESP grants 2013/07375-0 and 2016/24286-9, and CNPq grant 310893/2019-4. We are also indebted to LNLS for the beam time granted through proposal number 20160215 and to NVIDIA for the GPU used in the experiments, which was obtained through the NVIDIA Higher Education and Research Grants.

References

1. Aharon M, Elad M, Bruckstein A (2006) K-SVD: An algorithm for designing over-complete dictionaries for sparse representation. *IEEE Transactions on Signal Processing* 54(11):4311–4322, DOI 10.1109/TSP.2006.881199, 59749104367
2. Beck A, Teboulle M (2009) A fast iterative shrinkage-thresholding algorithm for linear inverse problems. *SIAM Journal on Imaging Sciences* 2(1):183–202, DOI 10.1137/080716542
3. Beck A, Teboulle M (2009) Fast gradient-based algorithms for constrained total variation image denoising and deblurring problems. *IEEE Transactions on Image Processing* 18(11):2419–2434, DOI 10.1109/TIP.2009.2028250
4. Bioucas-Dias JM, Figueiredo MAT (2007) A new TwIST: Two-step iterative shrinkage/thresholding algorithms for image restoration. *IEEE Transactions on Image Processing* 16(12):2992–3004, DOI 10.1109/TIP.2007.909319
5. Donoho DL (2006) Compressed sensing. *IEEE Transactions on Information Theory* 52(4):1289–1306, DOI 10.1109/TIT.2006.871582, URL http://ieeexplore.ieee.org/xpl/freeabs_all.jsp?isnumber=33885&arnumber=1614066&count=44&index=0
6. Drori Y, Teboulle M (2014) Performance of first-order methods for smooth convex minimization: a novel approach. *Mathematical Programming* 145(1–2):451–482, DOI 10.1007/s00365-007-9003-x
7. Engl HW, Hanke M, Neubauer A (2000) *Regularization of Inverse Problems*. Kluwer Academic Publishers
8. Erdoğan H, Fessler JA (1999) Ordered subsets algorithms for transmission tomography. *Physics in Medicine and Biology* 44(11):2835–2851, DOI <http://dx.doi.org/10.1088/0031-9155/44/11/311>
9. Garduño E, Herman GT (2017) Computerized tomography with total variation and with shearlets. *Inverse Problems* 33(4):44011–44024, DOI 10.1088/1361-6420/33/4/044011
10. Gong P, Zhang C, Lu Z, Huang JZ, Ye J (2013) A general iterative shrinkage and thresholding algorithm for non-convex regularized optimization problems. In: *Proceedings of the 30th International Conference on Machine Learning*, vol 28, pp 37–45, URL <https://dl.acm.org/doi/abs/10.5555/3042817.3042898>
11. Grippo L, Lampariello F, Lucidi S (1986) A nonmonotone line search technique for Newton’s method. *SIAM Journal on Numerical Analysis* 23(4):707–716, DOI 10.1137/0723046, URL <http://epubs.siam.org/doi/abs/10.1137/0723046>
12. Han G, Liang Z, You J (1999) A fast ray-tracing technique for TCT and ECT studies. In: *IEEE Nuclear Science Symposium Conference Record*, IEEE, 3, pp 1515–1518, DOI 10.1109/NSSMIC.1999.842846, URL http://ieeexplore.ieee.org/xpls/abs_all.jsp?arnumber=842846&tag=1
13. Herman GT (2009) *Fundamentals of Computerized Tomography: Image Reconstruction from Projections*, 2nd edn. Springer-Verlag, London
14. Herman GT, Meyer LB (1993) Algebraic reconstruction techniques can be made computationally efficient. *IEEE Transactions on Medical Imaging* 12(3):600–609, DOI 10.1109/42.241889, URL http://ieeexplore.ieee.org/xpl/freeabs_all.jsp?isnumber=6214&arnumber=241889&count=27&index=24
15. Herman GT, Garduño E, Davidi R, Censor Y (2012) Superiorization: An optimization heuristic for medical physics. *Medical Physics* 39(9):5532–5546, DOI 10.1118/1.4745566

16. Hiriart-Urruty JB, Lemaréchal C (1993) Convex Analysis and Minimization Algorithms. Springer-Verlag, Berlin
17. Kim D, Fessler JA (2015) An optimized first-order method for image restoration. In: IEEE International Conference on Image Processing, IEEE, pp 3675–3679, DOI 10.1109/ICIP.2015.7351490
18. Kim D, Fessler JA (2016) Optimized first-order methods for smooth convex minimization. Mathematical Programming 159(1-2):81–107, DOI 10.1007/s10107-015-0949-3, 1406.5468
19. Narayan TK, Herman GT (1999) Prediction of human observer performance by numerical observers: An experimental study. Journal of the Optical Society of America A 16(3):679–693, DOI 10.1364/JOSAA.16.000679
20. Nesterov YE (1983) A method for solving a convex programming problem with convergence rate $O(1/k^2)$. Soviet Mathematics Doklady 27(3):372–376
21. Nesterov YE (2004) Introductory Lectures on Convex Optimization: A Basic Course. Springer, New York
22. Parikh N, Boyd S (2014) Proximal algorithms. Foundations and Trends in Optimization 1(3):127–239, DOI 10.1561/2400000003
23. Taylor AB, Hendrickx JM, cois Glineur F (2017) Exact worst-case performance of first-order methods for composite convex optimization. SIAM Journal on Optimization 27(3):1283–1313, DOI 10.1137/16M108104X
24. Wright SJ, Nowak RD, Figueiredo MAT (2009) Sparse reconstruction by separable approximation. IEEE Transactions on Signal Processing 57(7):2479–2493, DOI 10.1109/TSP.2009.2016892
25. Yamagishi M, Yamada I (2011) Over-relaxation of the fast iterative shrinkage-thresholding algorithm with variable stepsize. Inverse Problems 27(10):105008, DOI 10.1088/0266-5611/27/10/105008
26. Zhang H, Hager WW (2004) A nonmonotone line search technique and its application to unconstrained optimization. SIAM Journal on Optimization 14(4):1043–1056, DOI 10.1137/S1052623403428208
27. Zibetti MVW, Lin C, Herman GT (2018) Total variation superiorized conjugate gradient method for image reconstruction. Inverse Problems 34(3):34001–340026, DOI 10.1088/1361-6420/aaa49b
28. Zibetti MVW, Helou ES, Regatte RR, Herman GT (2019) Monotone FISTA With Variable Acceleration for Compressed Sensing Magnetic Resonance Imaging. IEEE Transactions on Computational Imaging 5(1):109–119, DOI 10.1109/TCI.2018.2882681